Transonic buffet simulation using a partially-averaged Navier-Stokes approach

Andrea Petrocchi, George Barakos *

CFD Laboratory, School of Engineering, University of Glasgow, Glasgow, G128QQ, UK

ARTICLE INFO

ABSTRACT

The present article assesses the capability of the partially averaged Navier-Stokes (PANS) method to reproduce accurately the self-sustained shock oscillations, also known as transonic buffet, occurring on airfoils and wings at transonic regime under certain conditions of Mach number and angle of attack. The test case under analysis is an OAT15A unswept wing at Mach number $M_\infty = 0.73$ and Reynolds number $Re_c = 3 \times 10^6$. The three-dimensional flow is studied by accounting for the wind tunnel walls adopted in the experiments of Jacquin et al. [1] in the simulations. The computations on a large-span, confined configuration reveal a strong three-dimensionality of the flow both before and after the buffet onset. Attention is paid to the comparison with unsteady Reynolds-averaged Navier Stokes (URANS) results, to show the benefits of PANS in resolving flow unsteadiness at different flow resolutions, especially on affordable CFD grids, at limited additional cost. In this context, the role of the mesh metrics and the local turbulence level in the formulation of the model is described, as well as the relation of this latter with the spatiotemporal discretization used for the numerical simulations. The aim is to extend the use of PANS and obtain accurate predictions of flow cases involving shock-wave boundary layer interactions without expensive approaches.

1. Introduction

Computational fluid dynamics has been extensively used to simulate shock-wave/boundary-layer interaction (SBLI), especially at transonic conditions. Reynolds-averaged Navier Stokes (RANS) simulations have become the most popular tool in CFD because of their reduced CPU costs and wide range of applicability. Nevertheless, the prediction of SBLI phenomena with RANS simulations is not always accurate, especially when the flow is separated and presents strong shock oscillations. Following the increase in the availability of computational resources, direct numerical simulations (DNS) and large eddy simulations (LES) are no longer out of reach for canonical flows at moderate Reynolds numbers. Nevertheless, cases of aeronautical interest, e.g. the flow around transonic wings, cannot yet be studied with such high-resolution methods. Therefore, in recent years, hybrid RANS/LES approaches have been introduced to reduce the cost associated with the fine spatiotemporal discretization required from the aforementioned approaches.

In this context, the partially-averaged Navier-Stokes (PANS) [2] method was introduced as a bridging model between RANS and DNS. It resolves flow unsteadiness and flow structures where URANS predicts a steady behaviour or is only able to give a gross representation of the un-steady flow. The ratios of modelled-to-total turbulent kinetic energy and dissipation, f_k and f_ϵ, respectively, are introduced to control the filter width of the turbulence simulation. When both values are equal to unity the PANS equations are identical to RANS, whereas zero values of these parameters mean that the entire spectrum is resolved, i.e. DNS solution is obtained. The main advantage over URANS is that the resolution of a significant part of turbulent fluctuations is enabled, leading to an improved flow resolution. Such a feature is particularly useful for flows with separation, whether shallow separation or fixed-point separation. Buffet flows are in the former category since they exhibit an alternation of separation and reattachment. An advantage of PANS over other hybrid RANS/LES models is the potential to deliver improved results even adopting a RANS-like grid, as long as the values of the two parameters f_k and f_ϵ remain reasonably high [3]. Conversely, the switch to LES-mode of techniques like the DES family [4] in the separated region, reintroduces the requirements in terms of spatiotemporal discretization [5] present in LES computations, leading to a noticeable increase in the CPU costs.

---

* Corresponding author.

E-mail addresses: andrea.petrocchi@glasgow.ac.uk (A. Petrocchi), george.barakos@glasgow.ac.uk (G. Barakos).

Nomenclature

Latin Symbols

a_1	SST model constant	
c_p	specific heat at constant pressure	J/(kgK)
C_p	pressure coefficient $(p - p_\infty)/(0.5\rho U_\infty^2)$	
C_L	lift coefficient $L/(0.5\rho U_\infty^2 c)$	
C_{PANS}	PANS model constant	
e	internal energy per unit mass	$\mathrm{m^2/s^2}$
E	total energy per unit mass	$\mathrm{m^2/s^2}$
C_μ	model constant	
f_k	unresolved-to-total ratio of turbulent kinetic energy	
f_ϵ	unresolved-to-total ratio of turbulent dissipation	
f_ω	unresolved-to-total ratio of turbulent frequency	
F_1, F_2	SST model blending functions	
k	turbulent kinetic energy	$\mathrm{m^2 s^{-2}}$
k_h	heat transfer coefficient	$\mathrm{W\,m^{-1}\,K^{-1}}$
L_t	turbulent length scale	m
M	Mach number	
p	pressure	$\mathrm{kg\,m^{-1}\,s^{-2}}$
P_k	turbulent kinetic energy production term $\tau_{ij}\dfrac{\partial u_i}{\partial x_j}$	$\mathrm{kg\,m^{-1}\,s^{-3}}$
Pr	Prandtl number $\dfrac{\mu c_p}{k_h}$	
q	heat flux vector	$\mathrm{W\,m^{-2}}$
S	main strain rate tensor	$\mathrm{s^{-1}}$
St	Strouhal number $\dfrac{f c}{U_\infty}$	
t	time	s
T	temperature	K
T_S	Sutherland's temperature	K
R	flow residual vector	
Re_c	Reynolds number $\dfrac{\rho U_\infty c}{\mu}$	
U_i	flow velocity	$\mathrm{m\,s^{-1}}$
$V_{i,j,k}$	cell volume	
W	flow variable vector	
x_i	spatial coordinates	m

Greek Symbols

α	angle of attack	deg
Δ	characteristic grid size	m
$\Delta x, \Delta y, \Delta z$	grid size in the x, y, z directions	m
ϵ	turbulent dissipation	$\mathrm{m^2 s^{-3}}$
μ	molecular dynamic viscosity	$\mathrm{kg\,m^{-1}s^{-1}}$
μ_t	eddy viscosity	$\mathrm{kg\,m^{-1}s^{-1}}$
ω	turbulent frequency	$\mathrm{s^{-1}}$
ν_t	kinematic eddy viscosity	$\mathrm{m^2 s^{-1}}$
ρ	density	$\mathrm{kg\,m^{-3}}$
τ	viscous stress tensor	$\mathrm{kg\,m^{-1}s^{-2}}$
$\beta^*, \beta, \gamma, \sigma_k, \sigma_\omega$	SST model constants	

Acronyms

CFD	Computational Fluid Dynamics
DDES	Delayed Detached-Eddy Simulations
DES	Detached-Eddy Simulations
DNS	Direct Numerical Simulations
GCG	Generalized Conjugate Gradient
GMRES	Generalized Minimum Residual
HMB	Helicopter Multi-Block
IDDES	Improved Delayed Detached-Eddy Simulations
LES	Large-Eddy Simulations
MUSCL	Monotone Upstream-centered Scheme for Conservation Laws
PANS	Partially-Averaged Navier-Stokes
PSD	Power Spectral Density
RANS	Reynolds-Averaged Navier-Stokes
RMS	Root mean square
RSM	Reynolds-Stress Model
SAS	Scale-Adaptive Simulations
SBLI	Shock-wave/Boundary-Layer Interaction
SPL	Sound Pressure Level
SST	Shear Stress Tensor
URANS	Unsteady Reynolds-Averaged Navier-Stokes

So far, PANS simulations have been mainly tested on canonical flows in the incompressible formulation. Flows around circular [6–9] and square [10–12] cylinders, backward-facing steps [13], turbulent channels [14], or humps and hills [15–18] were mostly investigated. Rare exceptions are found in the works of Basu et al. [19] on transonic cavity flows, Luo et al. [20] on flows around a circular cylinder and ramped cavity at supersonic conditions, and the work of Bonnifet et al. [21] on transonic buffet. Early works are mostly based on the k-ϵ model as a RANS parent, while some others employed a k-ω closure. More recently, the formulation has been adapted to the Shear-Stress Transport model of Menter [22] and used by a number of authors [20,3,23,9]. Bonnifet et al. [21] adopted an RSM model while the group of Basara, Krajnovic et al. [14,24,12,25,26] proposed a four-equation model for a more accurate near-wall prediction. Only recently, PANS have been used for simplified flows of industrial appeal [27–30]. An overview of past studies adopting PANS is given in Appendix B.

Transonic buffet consists of self-sustained shock oscillations on aerofoils and wings in transonic regime due to unsteady shock-wave/boundary layer interaction. For extensive coverage of the topic, the reader is referred to the review paper of Lee [31] and, for recent developments, to the work of Giannelis et al. [32]. The presence of shock-induced separation triggering a self-induced flow instability makes the prediction of buffet with CFD very challenging, introducing questions about the performance of different turbulence models in the RANS context, and the superiority between the available hybrid RANS-LES approaches. The frequencies associated with the nearly periodic shock motion are about two orders of magnitude smaller than those associated with turbulence. Because of the large separation of scales and the need to compute several periods of oscillations, the presence of LES and DNS studies in the literature is still limited. A number of authors investigated the ability of turbulence models to capture buffet around two- and three-dimensional configurations [33–37]. Appendix A sees a brief recap of buffet simulations using URANS for the configuration of interest in this work. In spite of the large number of works documented in the literature, there is no consensus on the ability of URANS to predict buffet. This is influenced by a number of factors, like turbulence modelling, numerical schemes, spatiotemporal discretization, and test section. Therefore, many of the following works were carried out by using scale-resolving simulations by means of hybrid RANS/LES approaches like those of the DES family [4,38,39]. These techniques showed improved results in representing the buffet physics on two- [40,35,41,42] and three-dimensional [43–45] configurations. On the other hand, the CPU time associated with those simulations was significantly higher because of the requirements on the temporal and spatial discretization of the CFD domain.

Among the test cases used for buffet computations, the OAT15A airfoil has become particularly popular following the experimental campaign carried out at ONERA, for which the results were partially published in the work of Jacquin et al. [1]. The buffet flow displayed

some features of the conventional 2D buffet occurring on airfoils. Indeed, the periodic shock-induced separation and reattachment of the boundary layer were associated with a single frequency, corresponding to a Strouhal number of St = 0.06, which is in agreement with other works on 2D buffet. The study on the influence of the wind tunnel walls from Thiery and Coustols [37] also showed little difference in terms of average quantities. Nonetheless, the flow exhibits a more complex behaviour both pre- and post-buffet onset, showing a strong impact of the wind-tunnel walls and the large wingspan. In the first case, the shock front bends under the influence of the lateral tunnel walls in a way similar to that shown in the work of Garbaruk et al. [46]. This caused the shock position to be overpredicted by every turbulence model (see e.g. [35]) in the unconfined configuration. Moreover, the corner flow is not accounted for in 2D computations. At buffet conditions, the oil flow visualizations showed the presence of large 3D structures developing downstream of the shock, leading to an undulating shock front along the wingspan. A similar phenomenon, developing even on unswept wings, was underlined in the work of Iovnovich & Raveh [47] and Plante et al. [48] and takes the name of *buffet cells*. These structures exhibit the alternation of positive and negative pressure disturbances propagating in the spanwise direction. Subsequent works on swept and unswept, untapered wings in wind tunnels from Sugioka et al. [49] and Sansica et al. [50] showed the presence of the same flow topology observed by Jacquin et al. [1]. Large stall cells were recently observed for unswept configurations using periodic boundary conditions in the spanwise direction, e.g. in et al. [48,51]. In these cases, high aspect-ratio CFD models were used. In this view, we believe that the unconfined configuration with spanwise periodic boundary conditions and short spanwise extend, adopted in the majority of past CFD works, does not allow for a correct characterization of the buffet flow dynamics.

Among the past works on this test case, Deck [40] opted, for the first time, for a scale-resolving simulation, assessing the need for a zonal DES (ZDES). In his work, the basic version of DES failed in predicting the self-sustained shock motion, even well beyond the experimental onset. This technique did not lead to a satisfactory agreement with the experiments, because of over-prediction of the trailing edge unsteadiness. An analogous study using DDES of Grossi et al. [35] also showed a higher degree of unsteadiness predicted at the leading edge, although the prediction is improved with respect to the ZDES. An improvement was obtained with the use of OES by Szubert et al. [41]. These approaches share the need for an overly fine grid in the separated region that might be also seen as the cause for the wrong behaviour detected in this region. The same holds for the work of Huang et al. [42] where IDDES was employed. In their work, the timestep used was more than an order of magnitude higher than the other cases and this resulted in an overall wrong prediction of the shock position. The timestep size employed, possibly prevented the resolution of smaller structures and the reduced eddy viscosity caused an early separation, resulting in an upstream shock position. The failure when comparing the experimental results enforces the need for a temporal discretization that follows the spatial one. Even higher CPU times were needed for the few LES computations carried out so far [52–57]. Regardless, if computations of this type can be affordable for a simplified geometry, the cost becomes prohibitive for complex 3D cases. Therefore, it rises the need for a computational approach that is accurate for the prediction of the buffet without introducing the costs of the aforementioned approaches. Moreover, because of the reduced span adopted and the absence of the wind tunnel walls in the computation, none of the aforementioned works detected any of the 3D features displayed in the experiments. Therefore, we retain the wind tunnel walls in the computations to investigate the effect that they have on the 3D buffet physics and provide, eventually, a fair comparison with the experiments. The large span adopted should allow for the development of large vortical structures in the boundary layer as underlined in the experiments.

In this paper, we aim at investigating the ability of PANS to predict transonic buffet around the OAT15A airfoil as a compromise be-

tween URANS and other more expensive approaches like those of the DES family. Attention is paid to the efficiency of the computational method over URANS, and the capability of PANS to capture the correct flow physics at a reasonable CPU cost. Recent experiments from different research groups [58–61] provided new data for this configuration, pointing out differences with the previous investigation stemming from a modified experimental setup. Nevertheless, in this work, only the results of Jacquin et al. [1] will be used for comparison purposes. The article is structured as follows: in section 2 the compressible PANS formulation is presented with a focus on the different strategies adopted to estimate the PANS model parameters; section 3 is devoted to the method implementation in the Helicopter Multi-Block (HMB3) solver employed here; in section 4 the results for the flow around the OAT15A airfoil are presented before drawing some conclusions in section 5.

2. PANS formulation

The partially-averaged Navier-Stokes (PANS) formulation was introduced for the first time by Girimaji et al. [2] as a bridging model between RANS and DNS. This method is based on a RANS paradigm, where the blending is obtained by means of the user-prescribed unresolved-to-total ratios of turbulent kinetic energy f_k and dissipation f_ϵ, bounded between 0 and 1, acting on the turbulence closure equations. They read:

$$f_k = \frac{k_u}{k}, \quad f_\epsilon = \frac{\epsilon_u}{\epsilon},$$ (1)

where the u subscripts stand for the unresolved portions of quantities, and the denominators are the totals. The PANS method was initially derived for k-ϵ closures and then extended to the Wilcox k-ω model [62] by Lakshmipathy et al. [8] and to the Menter SST model [22] by Luo et al. [20]. In k-ω based formulations the parameter f_ϵ is replaced by the unresolved-to-total turbulence frequency f_ω through the following relation:

$$f_\omega = \frac{\omega_u}{\omega} = \frac{f_\epsilon}{f_k}.$$ (2)

These formulations inherit from the parent RANS models an eddy viscosity based on a Boussinesq approximation, that is reduced with respect to the RANS case because of the effects of the f_k parameter: since only a fraction of the turbulent kinetic energy is modelled, the corresponding value of the eddy viscosity is reduced. This gives the possibility for the turbulent structures to be resolved. Alternative formulations like those in ref. [25,24], based on a k-ϵ-ζ-f model, and the PANS-RSM approach of Bonnifet et al. [21].

In this work the SST-PANS formulation is adopted:

$$\frac{\partial(\rho k)}{\partial t} + \frac{\partial(\rho U_j k)}{\partial x_j} = P_k - \beta^* \rho k \omega + \frac{\partial}{\partial x_j}\left[\left(\mu + \mu_t \sigma_k \frac{f_\omega}{f_k}\right)\frac{\partial k}{\partial x_j}\right],$$ (3)

$$\frac{\partial(\rho \omega)}{\partial t} + \frac{\partial(\rho U_j \omega)}{\partial x_j} = \frac{\gamma}{\nu_t} P_k - \beta' \rho \omega^2 + \frac{\partial}{\partial x_j}\left[\left(\mu + \mu_t \sigma_\omega \frac{f_\omega}{f_k}\right)\frac{\partial \omega}{\partial x_j}\right]$$
$$+ 2\frac{f_\omega}{f_k}(1 - F_1)\frac{\rho \sigma_{\omega 2}}{\omega}\frac{\partial k}{\partial x_j}\frac{\partial \omega}{\partial x_j},$$ (4)

where ρ is the density, U_j is the flow velocity, μ is the dynamic molecular viscosity, and μ_t is the turbulent viscosity. Here, the turbulent kinetic energy k and frequency ω are the modelled, or unresolved, fractions where the subscripts were dropped for simplicity. In the ω-equation, $\beta' = \left(\gamma\beta^* - \frac{\gamma\beta^*}{f_\omega} + \frac{\beta}{f_\omega}\right)$; F_1 is the blending function while $\gamma, \beta, \beta*, \sigma_k, \sigma_\omega$ are the model constants, calculated as prescribed in reference [22]. The turbulent viscosity is calculated as

$$\mu_t = \min\left(\frac{\rho k}{\omega}; \frac{\rho a_1 k}{SF2}\right),$$ (5)

where S is the main strain rate tensor, F_2 is a second blending function and a_1 is equal to 0.31.

2.1. Estimate of f_k

A debated point is how to prescribe the value of f_k [23]. Three main approaches are distinguished here:

- *Constant* f_k, where the parameter is not dependent on space and time;
- *Static* f_k, where an optimal distribution is found after a preliminary steady RANS simulation;
- *Dynamic* f_k, where the parameter is a function of space and updated over time.

There is no consensus on which of these three approaches should be used; the *Constant* approach is preferred by its advocates because adopting a spatially and temporally constant filter, modelling and discretization errors can be quantified. On the other hand, since the value of the parameter is not known *a priori*, a sensitivity study is required. Moreover, for flows where confined regions of high turbulent content and anisotropies in the grid are present, e.g. boundary layers, this approach does not seem reasonable. Conversely, a variable filter allows an optimal usage of resources since it usually adapts to both the turbulent content and the local grid size. Many estimates were proposed over time, and again no consensus was found. Moreover, comparing *Static* and *Dynamic* approaches, it is clear how the latter introduced some additional CPU costs due to the dynamic evaluation of f_k over the former, as well as, the *Constant* approach. The implementation ease is also reduced. That is the reason why a *Static* approach is more suitable for problems with localized statistically steady turbulence, whereas the *Dynamic* approach is required when coming to intrinsically unsteady flows like for the case of buffet flows, and hence is adopted in this work.

The f_ϵ parameter is usually set to one, under the assumption that all dissipative scales are not resolved in the computation. This approach is suitable for high Reynolds numbers for which there is a net separation between energy-containing and dissipative scales [2]. The estimates adopted in this work are:

$$f_k = C_{\text{PANS}} \left(\frac{\Delta}{L_t} \right)^{2/3}, \tag{6}$$

$$f_k = \frac{1 + \tanh(2\pi(\Lambda - 0.5))}{2}, \Lambda = \frac{1}{1 + \left(\frac{L_t}{\Delta} \right)^{4/3}}, \tag{7}$$

where $L_t = \sqrt{k}/(C_\mu \omega)$ is the local turbulent length scale, and Δ is the local grid size. The constant C_{PANS} is reduced with respect to the value of $1/\sqrt{C_\mu}$ prescribed for static estimates. Since the turbulent length scale is not based on total quantities, like in the case of estimates based on preliminary RANS calculations, it is reduced and, in turn, f_k is overly increased.

2.2. Estimate of Δt

While many estimates were given for the f_k parameter, not many sensitivity studies to determine the correct timestep are present in the literature. For the specific case, the timestep can be chosen as a suitable fraction of the buffet period to describe adequately the time evolution of the flow. At the same time, the turbulence Strouhal number, or frequency, is much higher than the dominant one and this also helps in the choice of Δt. An estimate of this flow feature can be given a posteriori from the spectral energy content in sensitive regions of the flow field. Here, nevertheless, a relation similar to that between f_k and Δ is given to determine the right timestep. An unresolved Kolmogorov time scale can be determined only considering modelled quantities, and related to the RANS time scale $1/(c_\mu \omega)$ by means of f_k through the following:

$$t_{ku} = (\nu_u / \epsilon_u)^{1/2} = \sqrt{C_\mu f_k} \frac{1}{\omega} . \tag{8}$$

Again, the local optimal timestep is influenced by the local turbulence and the grid size by means of f_k. The above estimate can also be used to evaluate which scales can be solved with the current resolution. The idea is to choose the minimum value of t_{ku} over the computational domain and set it as Δt. In practice, the boundary layer must be neglected in this process, because the estimate goes to zero in the vicinity of the walls, where the turbulent specific dissipation reaches high values.

3. Implementation in HMB3

The PANS method was implemented in the helicopter multi-block (HMB) solver of the University of Glasgow [63,64], a three-dimensional, fully implicit code for the solution of the Navier-Stokes equations, reading:

$$\frac{\partial \rho}{\partial t} + \frac{\partial}{\partial x_i} \left(\rho u_i \right) = 0,$$

$$\frac{\partial \rho u_i}{\partial t} + \frac{\partial}{\partial x_j} \left(\rho u_i u_j \right) = \rho f_i - \frac{\partial p}{\partial x_i} + \frac{\partial \tau_{ij}}{\partial x_j},$$

$$\frac{\partial \rho E}{\partial t} + \frac{\partial}{\partial x_j} \left[u_j \left(\rho E + p \right) \right] = \frac{\partial}{\partial x_j} \left(u_i \tau_{ij} - q_j \right) . \tag{9}$$

In the continuity equation, ρ is the density, u_i is the velocity field, and t is time. The momentum equations introduce the pressure p, body forces f_i, and the viscous stress tensor τ_{ij}. In the energy equation, E is the total energy per unit mass, and q_j is the heat flux vector. The total energy per mass unit $E = e + u_i u_j/2$ is the summation of internal energy per unit mass e and kinetic energy per unit mass. For Newtonian fluids, under the assumption of Stokes' hypothesis, the viscous stress tensor is written as:

$$\tau_{ij} = \mu \left[\left(\frac{\partial u_i}{\partial x_j} + \frac{\partial u_j}{\partial x_i} \right) - \frac{2}{3} \delta_{ij} \frac{\partial u_k}{\partial x_k} \right], \tag{10}$$

where μ is the molecular dynamic viscosity and δ_{ij} is the Kronecker delta. The molecular viscosity is evaluated through the Sutherland Law:

$$\mu = \mu_0 \left(\frac{T}{T_0} \right)^{3/2} \frac{T_0 + T_S}{T + T_S} \tag{11}$$

where μ_0 is a reference viscosity at the reference value T_0, while T_S is the Sutherland's temperature. Throughout the following investigation, the adopted values are $\mu_0 = 1.7894 \times 10^{-5} \text{kg}/(\text{m s})$, $T_0 = 288.16\text{K}$ and $T_S = 110.4\text{K}$. In the energy equation, the heat flux vector is computed using Fourier's Law for thermal conduction:

$$q_j = -k_h \frac{\partial T}{\partial x_j}, \tag{12}$$

where k_h is the heat transfer coefficient. The laminar Prandtl number Pr (0.72 in this work) is used to recast the equation, that now reads:

$$q_j = -\frac{c_p \mu}{\text{Pr}} \frac{\partial T}{\partial x_j} . \tag{13}$$

c_p is the heat capacity at constant pressure. Under the assumption of ideal gas, the state equation links pressure and density and is used to close the system of equations:

$$p = \rho R_{air} T, \tag{14}$$

where the ideal gas constant for air is $R_{air} = 287.058 \text{ J}/(\text{kg K})$.

The Navier-Stokes equations are discretized using a cell-centerd finite volume approach. The computational domain is divided into a finite number of non-overlapping control-volumes, and the governing equations are applied to each cell. Also, the Navier- Stokes equations are re-written in a curvilinear coordinate system which simplifies the formulation of the discretized terms since body-conforming grids are
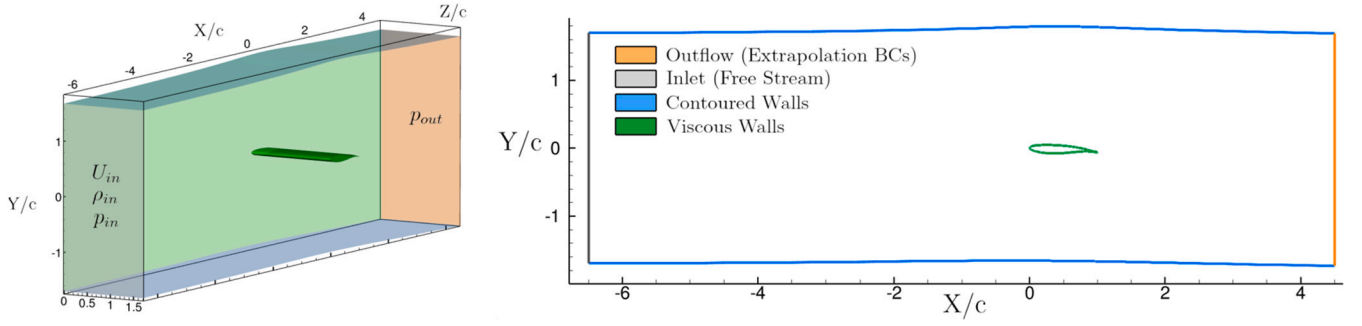
Fig. 1. Computational domain with coloured by boundary conditions. The symmetry plane at $z/c = 1.7$ is not coloured.

adopted here. The spatial discretization of the equations leads to a set of ordinary differential equations in time,

$$\frac{d}{dt}(\mathbf{W}_{ijk}V_{ijk}) = -\mathbf{R}_{ijk}(\mathbf{W}), \tag{15}$$

where $\mathbf{W}$ and $\mathbf{R}$ are the vectors of cell conserved variables and residuals respectively. The convective terms are discretized using Osher's upwind scheme [65]. MUSCL variable extrapolation [66] is used to provide second-order accuracy with the Van Albada limiter [67] to prevent spurious oscillations around shock waves. The integration in time of the previous equation to a steady-state solution is performed using an implicit time-marching scheme. In the turbulent case, the state vector embodies k and ω. The linearized system of equations is solved using the generalized conjugate gradient method with a block incomplete lower–upper (BILU) factorization as a pre-conditioner [68]. The solver offers several one-equation, two-equation, three-equation, and four-equation turbulence models. In addition, LES, DES, delayed DES (DDES), improved DDES (IDDES), SAS and PANS methods are also available.

Since PANS is based on a RANS paradigm, the main modification consists of the addition of f_k in the diffusion terms, the destruction term in the ω-equation and the cross-diffusion term. The turbulent length scale is computed through the local values of the turbulent kinetic energy and specific dissipation. Different characteristic grid sizes can be considered. The available options are the maximum grid size $\Delta_{\max}$, the minimum grid size $\Delta_{\min}$, the L2-norm Δ_{L2}, or cell diagonal, and the cubic root of the cell volume Δ_{vol}. They read:

$$\Delta_{\max} = \max(\Delta x, \Delta y, \Delta z), \tag{16}$$

$$\Delta_{\min} = \min(\Delta x, \Delta y, \Delta z), \tag{17}$$

$$\Delta_{L2} = \sqrt{\Delta x^2 + \Delta y^2 + \Delta z^2}, \tag{18}$$

$$\Delta_{\mathrm{vol}} = \sqrt[3]{\Delta x \Delta y \Delta z}. \tag{19}$$

The turbulent length scale is clipped to 10^{-10} to avoid division by zero in the boundary layer. A feature to clip f_k between a minimum and maximum value has also been added to the code. The maximum value is always 1 since the estimate adopted does not prevent the parameter to exceed unity, while the minimum value can be tuned by the user. Nevertheless, too low values of f_k correspond to a significant reduction of the eddy viscosity that must be followed by a reduction of both the spatial and temporal discretization. Moreover, excessively small values of this parameter can compromise the stability of the computation and increase the CPU costs. The role of the minimum f_k will be investigated in the next section. As an alternative, the constant approach can be used, and a fixed value can be stored in the memory, avoiding the need to recompute the two length scales.

Exploiting the capability of the solver to work with multi-block grids, it was possible to enable the zonal approach setting $f_k = 1$ a priori in selected blocks. This allows the solver to skip the PANS routine in blocks where a RANS behaviour is expected.

4. Results

4.1. Experimental test case description

In the present study, the flow around the supercritical aerofoil OAT15A is investigated, that was studied experimentally by Jacquin et al. [69,1] in the S3Ch wind tunnel at ONERA. The wing section had a chord of $c = 0.23$m and a span, coinciding with that of tunnel, of 0.78 m. The section had a thickness-to-chord ratio of $t/c = 0.123$ and a trailing edge thickness of 0.5% of the chord. The wing was mounted in a squared section wind tunnel having nominal dimensions of 0.78m $\times$ 0.78m $\times$ 2.2m. An adaptation technique based on a steady flow hypothesis was used at the lower and upper walls to reproduce free-stream conditions, hence to minimise the interference of the facility on the aerofoil. Measurements were collected at free-stream Mach numbers in the range of 0.7-0.75, a chord-based Reynolds number of $\mathrm{Re}_c = 3 \times 10^6$ and angle of attack in the range of 1.36 - 3.9 degrees. The adoption of static pressure measurements and Kulite sensors distributed in the vicinity of the mid-span section allowed to detect the occurrence of flow unsteadiness at an angle of attack of 3.1 degrees, culminating in a self-sustained shock-induced oscillation at an angle of 3.5 degrees. For the case at M = 0.73 and $\alpha = 3.5$ degrees, a laser Doppler velocimetry (LDV) system was used to acquire velocity-field data and compute statistics. At all other flow conditions the pressure measurements were enriched with oil-flow and schlieren visualizations.

In this work, the study is mainly focused on conditions with constant Mach number M = 0.73 and angles of attack of $\alpha = 2.5$, 3.5 and 3.9 degrees, representative of a statistically steady flow and two fully-established buffet flows, respectively.

4.2. CFD grids and numerical setup

Two configurations were analyzed. The first one, denoted 3D in Table 2, is a reproduction of half of the wind tunnel used in the experimental campaign (see Fig. 1). The grids adopted for this configuration are indicated as C3, M3, and F3 in Table 1.

The upper and lower walls were modelled as slip-walls, and the shape was extracted from a preliminary 2D RANS simulation to replicate the results of the adaptive technique used in the experimental campaign. The upper and lower wall shape is shown in Fig. 1, right. In the study of Thiery and Coustols [37] the comparison between the confined and unconfined cases showed some differences in the computed mean velocity profiles and it is the main reason for accounting for the wind tunnel walls. As the adaptive walls in the experiments are shaped as streamlines, the adoption of slip conditions seems reasonable. The latter also allows for saving grid points required for the discretisation of a viscous boundary layer. Moreover, the separated flow region at the wing-wall junction triggers a three-dimensional behaviour that is not present in quasi-2D configurations with periodic boundary conditions with reduced spans [42,35,41].

The second configuration is called 2D in Table 2 and M2 in Table 1, and it was used for 2D preliminary computations. The aerofoil is no

Table 1
Main features of the different grids used for computations.

Grid #	$N_{aerofoil}$	N_z	$\Delta z_{wall}/c$	$\Delta z_{max}/c$	N_y	$\Delta n_{aerofoil}/c$	$\Delta z_{walls}/c$	N_{wake}	$\Delta x_{TE}/c$	N_{tot}
M2	470	-	-	-	115	5×10^{-6}	-	220	5×10^{-6}	1.10×10^5
C3	405	76	2×10^{-6}	0.033	102	5×10^{-6}	5×10^{-3}	86	5×10^{-6}	$\simeq 5.03 \times 10^6$
M3	500	100	2×10^{-6}	0.025	114	5×10^{-6}	5×10^{-3}	120	5×10^{-6}	$\simeq 10 \times 10^6$
F3	510	164	2×10^{-6}	0.015	128	5×10^{-6}	5×10^{-3}	150	5×10^{-6}	$\simeq 16.70 \times 10^6$

Table 2
Computations performed at different angles of attack, on different grids, and using different timesteps. All computations are at $M_\infty = 0.73$ and $Re_c = 3 \times 10^6$. In the run ID, U stands for URANS, and P for PANS.

Run #	α	2D/3D	Mesh	f_k	$f_{k,\text{inf}}$	Δt	x_{tr}/c	$P_{\text{out}}/P_{\text{in}}$	Buffet
R2M25	2.5	2D	M2	-	-	steady	fully turb.	1.0	No
R3C25	2.5	3D	C3	-	-	steady	fully turb.	1.0	No
R3M25	2.5	3D	M3	-	-	steady	fully turb.	1.0	No
R3F25	2.5	3D	F3	-	-	steady	fully turb.	1.0	No
P2M25	2.5	2D	M2	$f_k = 0.7$	-	0.1	fully turb.	-	No
P3C25a	2.5	3D	C3	eq. (6)	0.6	0.1	fully turb.	1.0	No
P3C25b	2.5	3D	C3	eq. (7)	0.6	0.1	fully turb.	1.0	No
P3C25c	2.5	3D	C3	eq. (7)	0.6	0.025	fully turb.	1.0	No
P3C25d	2.5	3D	C3	eq. (7)	0.6	0.025	fully turb.	0.99	No
U3M25	2.5	3D	M3	1.0		0.025	fully turb.	1.0	No
P3M25a	2.5	3D	M3	eq. (7)	0.6	0.025	fully turb.	1.0	No
P3M25b	2.5	3D	M3	eq. (7)	0.6	0.01	fully turb.	1.0	No
P3M25c	2.5	3D	M3	eq. (7)	0.6	0.01	fully turb.	0.99	No
U3F25	2.5	3D	F3	1.0		0.025	fully turb.	1.0	No
P3F25a	2.5	3D	F3	eq. (7)	0.6	0.1	fully turb.	1.0	No
P3M25b	2.5	3D	F3	eq. (7)	0.6	0.01	fully turb.	1.0	No
P3M25c	2.5	3D	F3	eq. (7)	0.6	0.005	fully turb.	1.0	No
U3C35a	3.5	3D	C3	-	-	0.01	fully turb.	-	No
U3C35b	3.5	3D	C3	-	-	0.01	0.07	0.99	No
P2M35a	3.5	2D	M2	$f_k = 0.7$	-	0.01	fully turb.	-	Yes
P2M35b	3.5	2D	M2	$f_k = 0.7$	-	0.01	0.07	-	Yes
P3C35a	3.5	3D	C3	eq. (6)	0.4	0.01	fully turb.	1.0	Yes
P3C35b	3.5	3D	C3	eq. (7)	0.4	0.01	fully turb.	1.0	Yes
P3C35c	3.5	3D	C3	eq. (7)	0.4	0.01	fully turb.	0.99	Yes
P3C35d	3.5	3D	C3	eq. (7)	0.4	0.01	0.07	0.99	Yes
P3C35d	3.5	3D	C3	eq. (7)	0.4	0.01	0.25	0.99	Yes
P3C35e	3.5	3D	C3	eq. (7)	0.6	0.01	0.07	0.99	Yes
P3M35a	3.5	3D	M3	eq. (7)	0.6	0.01	0.07	0.99	Yes
P3M35b	3.5	3D	M3	eq. (7)	0.6	0.005	0.07	0.99	Yes
P3F35	3.5	3D	F3	eq. (7)	0.6	0.005	0.07	0.99	Yes
U2M39	3.9	2D	M2	-	-	0.1	fully turb.	-	No
P2M39	3.9	2D	M2	$f_k = 0.7$	-	0.1	fully turb.	-	Yes
P3C39a	3.9	3D	C3	eq. (7)	0.4	0.01	0.07	0.99	Yes
P3C39b	3.9	3D	C3	eq. (7)	0.6	0.01	0.07	0.99	Yes

longer confined and freestream values are applied at the far field, distant 80c from the aerofoil.

The solid walls were treated using adiabatic, no-slip conditions. The normal spacing adopted was such to satisfy the condition on $\Delta y^+ < 1$. In both cases, at the aerofoil trailing edge, the same first cell spacing was used in both the normal and longitudinal direction in order to adequately describe the vortex detachment. At the solid sidewalls, the normal spacing is slightly finer than that on the aerofoil to obtain a value of Δy^+ below 1. The spacing on the slip walls is significantly coarser than that on the viscous walls. For the unsteady simulations, the convergence of the implicit scheme was based on the reduction of the flow field residual (by 3 orders of magnitude) with respect to the previous step. A maximum of 150 inner iterations were computed for each timestep.

4.3. Initial 2D study

An initial study on the 2D configuration was carried out. For this case, a constant formulation of $f_k = 0.7$ was adopted. This helped in the prediction of the shock oscillation, compensating for the inability of the SST model to predict buffet in this case and condition, as al-

ready documented in [70,71]. The effect of the inflow turbulence value, sustainability term, and laminar-to-turbulence transition were investigated. Fig. 2 reveals how the addition of the transition at the 7% of the chord allows for a better prediction of the RMS peak and trailing edge RMS. The sustainability term of Spalart and Rumsey [72], on the other hand, leads to a slightly upstream shock position and a high level of unsteadiness at the trailing edge. Because of the limited extent of the wind tunnel configuration, this correction was not applied in the following 3D study. The level of free-stream turbulence does not play a major role in the prediction of the mean shock position and slightly influences the peak value of the RMS. In conjunction with transition fixed at $x_{tr}/c = 0.07$, a turbulent-to-molecular eddy viscosity ratio of 10 led to the best agreement with the experiments and was used for the following 3D campaign.

4.4. Pre-buffet flow

In principle, scale resolving simulations (SRS) should be able to recover the RANS solution if this latter predicts the flow with a certain degree of accuracy. Because of the higher accuracy of SRS, the results may depart from RANS, especially if the flow is highly unsteady. For the
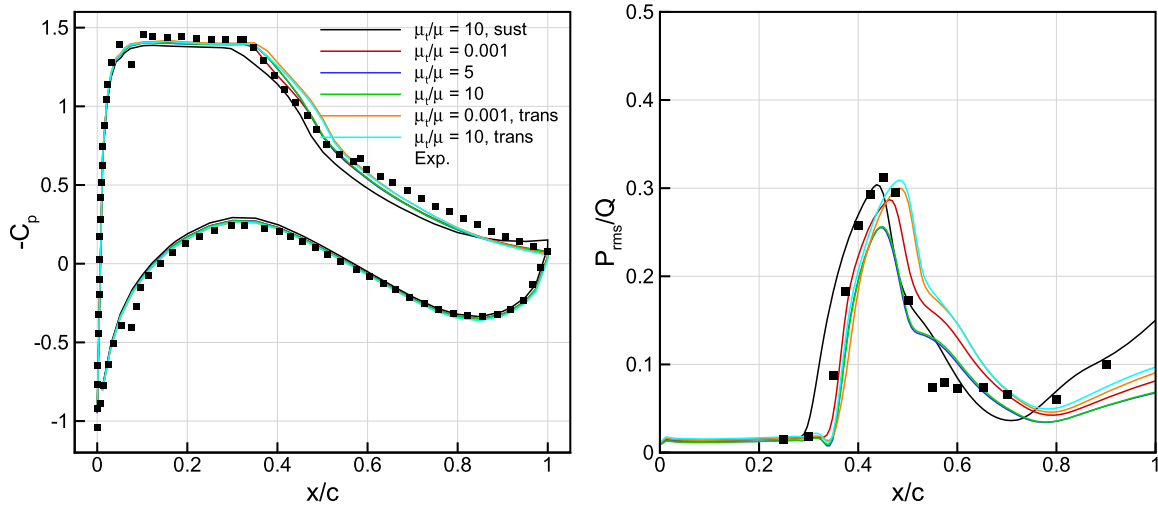
Fig. 2. Left: time-averaged pressure coefficient at $\alpha = 3.5$ deg; right: root means square of the pressure. Experiments from [1].
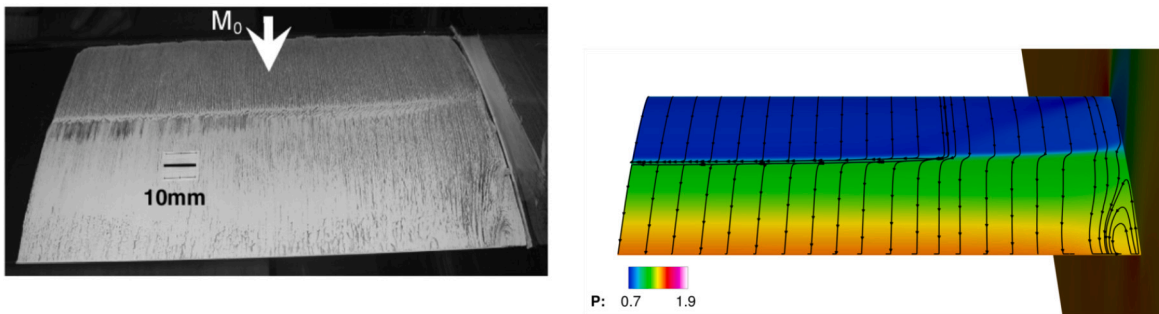

Fig. 3. Left: oil flow visualization around the OAT15A (picture taken from [1]) at $\alpha = 2.5$ deg; right: friction lines and surface pressure contour from CFD.

statistically steady flow at $\alpha = 2.5$ deg, the aim is to recover the RANS solution, within a certain tolerance, with the use of PANS.

Fig. 3, right plot, is taken from the converged URANS solution and underlines one of the challenges of this test case by displaying the friction lines and surface pressure contour. The shock position can be detected by the negative values of the streamwise component of the stress tensor at the surface or, going toward the sidewall, from a sudden deflection of the friction lines. As the flow here exhibits a small separation at the shock foot, the pressure contour helps locate the shock. The shock bends when approaching the sidewalls because of viscous effects. Together with this, a region of separated flow is confined within 10% of the span, in agreement with the experimental results in the left image.

Moreover, because of the viscous sidewall, the turbulence level in the boundary layer grows as it approaches the aerofoil. This coincides with a growth in the turbulence length scales and a following reduction of f_k at the wall. In principle, the behaviour of the method is correct since f_k is lowered in regions of high turbulence content, but in this case, it would require a smaller timestep to resolve all flow structures developing at the wall-aerofoil junction. Therefore, we exploited the multi-block grid to impose a RANS treatment in the very first layer of blocks on the wall. This avoids unnecessary costs to discretize the sidewall region. This is further justified by the experiments, stating that the separated flow region extent was almost constant over a buffet period.

Fig. 4 shows the comparison of the pressure coefficient C_p around the aerofoil with the experiments. The pressure was extracted at the same location of the pressure sensors used in the wind tunnel model. The left plot shows the results from URANS computations on different grids. Fig. 5 shows the same quantities for PANS simulations using the estimate in eq. (7) with $f_{k,\inf} = 0.6$ and different grids. The back pressure was here reduced by 1% with respect to the inlet value. This
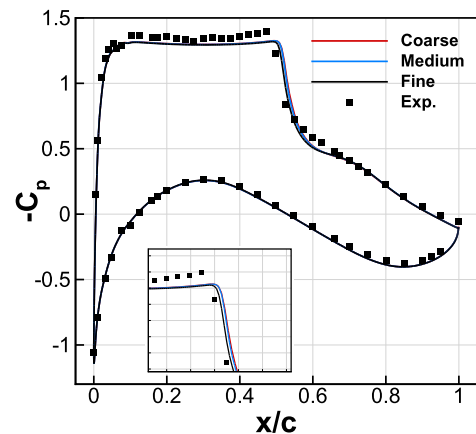

Fig. 4. Pressure coefficient around the OAT15A at $\alpha = 2.5$ deg using URANS. Experiments of [1].

choice is motivated by the work of Thiery and Coustols [37], which shows experimental and numerical results for the case under analysis. In the current work, the shock position is slightly influenced by the grid adopted. As the adopted estimate accounts for the local grid size, f_k is lowered for finer grids. This results in a slight difference in the shock position, as a reduced eddy viscosity promotes boundary layer separation. A lower back pressure results in a pressure gap on both sides of the aerofoil. Nevertheless, a pressure difference between the inlet and outlet sections is required to counteract the viscous effect of the wind tunnel walls. By imposing such a difference, shock oscillations are also promoted.
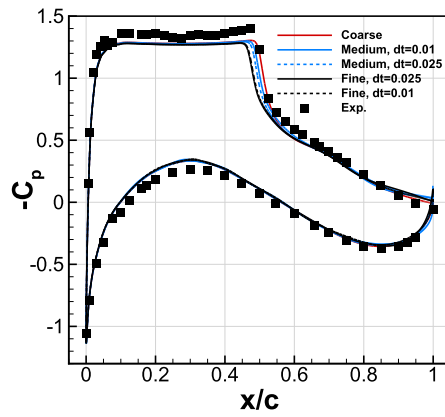
Fig. 5. Pressure coefficient around the OAT15A at $\alpha = 2.5$ deg using PANS. Experiments of [1].

4.5. Developed buffet flow

The buffet case is now investigated. Several simulations were performed at $\alpha = 3.5$ and 3.9 degrees, using different grids and time steps. The effect of some parameters was investigated to find the correct simulation setup. In particular, the wind tunnel back pressure was varied. Moreover, the comparison between the estimates of f_k introduced in the previous section is shown. Boundary layer tripping location and clip of f_k were modified. The main results are shown in Appendix C. Where not specified, the coarser grid in Table 1 was used as it proved able to correctly predict the oscillatory behaviour of the solution. A comparison with finer grids is then shown.

4.5.1. f_k investigation

Here the different f_k distributions were compared. A previous study [71] revealed that the optimal value of C_{PANS} for the actual configuration and grid size is 0.5 when the estimate of eq. (6) is used. That value allowed for the desired reduction of eddy viscosity in the region around the trailing edge and the formation of two distinct separated flow regions, one at the wing-wall junction and the other at the trailing edge. Higher values of the constant resulted in the absence of boundary layer separation at the centreplane and in an overprediction of the corner separation size. Fig. 6 shows the comparison between the f_k distributions provided by the two estimates. The similar behaviour obtained allowed us to conclude that the model of Elmiligui et al. [7], at least for the case under analysis, is a better option because it does not need the calibration of any parameter. The modelled-to-total ratio of turbulent kinetic energy reacts to regions of high turbulent content and acts by lowering the level of eddy viscosity while it assumes values close to 1 in the boundary layer and the far field region, i.e. switching the formulation to RANS. The estimate of eq. (7) also guarantees a slightly later transition from the RANS region in the boundary layer with respect to that of eq. (6). As the desired value of f_k in the boundary layer is 1, this latter is a factor of merit. Moreover, the estimate of eq. (6) can exceed 1 in the far field, while that of eq. (7) is bounded between 0 and 1 by definition. The latter is seen as a minor issue as f_k can be clipped, as specified in section 2. For these reasons, the estimate in eq. (7) was adopted in the following sections.

4.5.2. Back pressure influence

The wind tunnel back pressure value also plays a role in the correct prediction of this phenomenon, unlike unconfined configurations where the free stream is far away from the aerofoil and the influence is reduced. Since the exact value is not available from the experiments, we had to investigate the role of this parameter. The adopted values of the back pressure were equal to and 99% of the inlet pressure, denoted $BP = 1$ and $BP = 0.99$, respectively, in Fig. 7. The lower the back

pressure, the larger the amplitude of oscillations. Moreover, because of the viscous sidewall, some losses are introduced and there is a need for lower back pressure with respect to the inflow one. In the work of Thiery and Coustols [37], the numerical and experimental wind tunnel pressure on the upper and lower wall showed a drop between inlet and outlet of around 1%. This motivated our choice of the back pressure. The application of such correction results in an increase in the shock oscillation amplitude and pressure RMS (see Fig. 7) all over the wing section.

4.5.3. Study on different resolutions

Here the role of the mesh was investigated. The Q-Criterion iso-surface in Fig. 8 shows that the approach enables the unsteadiness associated with the buffet and is able to describe structures with increasing resolution as the grid size increases. The finer grid was employed with a reduction of the time step to one-half of the initial one. Employing the coarse mesh, the resolution was not enough to capture the motion at smaller scales. The spanwise discretization of the C3 grid did not allow the resolution of smaller structures associated with the turbulence in the separated region and the wake. Moreover, the adoption of a coarse grid did not allow the development of any 3D structures in the separated boundary layer. The medium grid helped resolve an increased number of structures, mainly spanwise vortex shedding, at the trailind edge. Using the finer grid, it was possible to predict the same flow topology of the experiments [1]. From this, we conclude that the spanwise discretization adopted in the coarse grid is not enough to capture all the correct flow physics. In this case, although the boundary layer is separated from the shock foot to the leading edge, the structures generated under the influence of the sidewall cannot propagate towards the center of the tunnel. The case is analogous to the computation of Thiery and Coustols [37], where the flow oscillation was predicted and just a hint of flow three-dimensionality was shown through friction lines. In that case, possibly because of the use of a RANS-like grid, stall cells could not be established along the span. The buffet dynamics will be discussed in further detail in the following.

In all cases, the overall agreement with the experiments of C_p and P_{RMS}, shown in Fig. 9 is satisfactory. The mean shock position slightly moved upstream when a finer grid was used. This effect was mainly due to the non-uniform shock front and the presence of the stall cells on the suction side of the wing. Moreover, the finer grid adopted at the trailing edge, together with the smaller timestep, allowed for the resolution of smaller scales and an increase in the level of fluctuations. This was also beneficial in terms of agreement of the mean pressure coefficient. A slight gap in terms of pressure coefficient is present on both sides ($\Delta C_p < 0.06$ on the suction side and $\Delta C_p < 0.08$ on the pressure side). This is possibly due to the lack of knowledge of the experimental setup and differences in the adaptive wall shape between the experiments and the CFD simulations.

The analysis in the following chapter was performed with data from the simulation P3F35 of Table 2.

4.5.4. Mean quantities

In the previous section, the average pressure coefficient and pressure RMS were shown. Here, also the mean longitudinal component of the velocity and the RMS are shown in Fig. 10 and Fig. 11, respectively. In all computations, the statistics were computed over several buffet periods (a minimum of 3). Accounting for the last buffet period always led to insignificant changes in the flow statistics. The probes were located at the same position as in the LDV measurements, i.e. around $z/c = 1.32$, where $z = 0$ is the sidewall and $z/c = 1.7$ is the symmetry plane. The pressure differences shown in the previous section coincide with the velocity differences outside of the boundary layer, particularly evident at $x/c = 0.45$. The slightly upstream shock position reflects in a difference in the RMS peak at $x/c = 0.45$, while the agreement is remarkable on the second part of the aerofoil. At $x/c = 0.28$, since the fluctuations in the boundary layer are not resolved, the RMS is practically zero, unlike
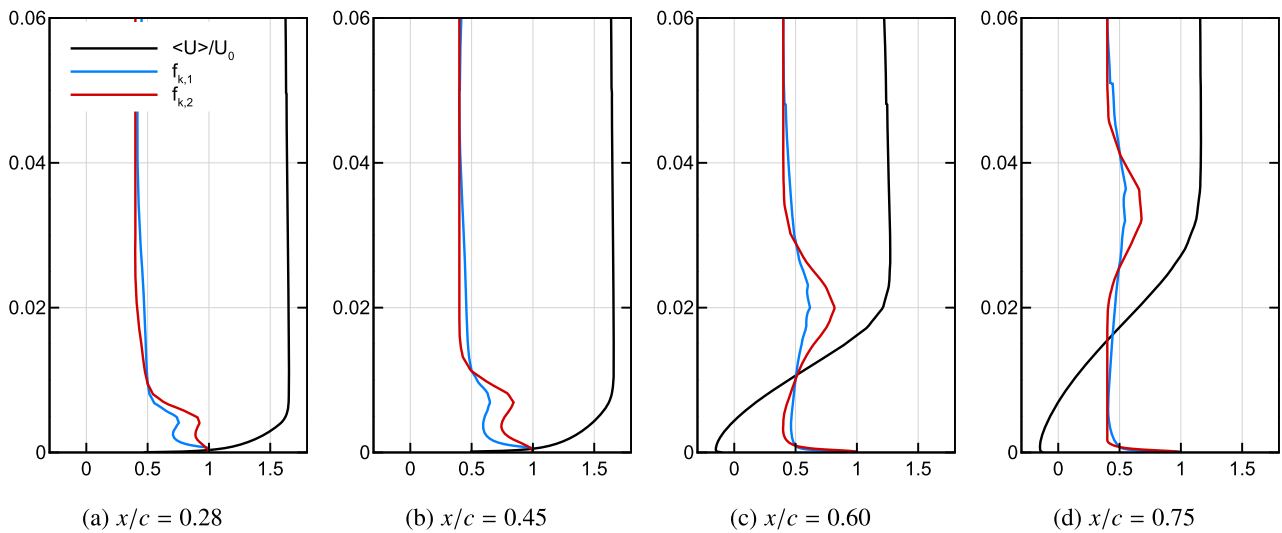
(a) $x/c = 0.28$ (b) $x/c = 0.45$ (c) $x/c = 0.60$ (d) $x/c = 0.75$

Fig. 6. Instantaneous profiles of horizontal velocity, turbulent-to-molecular viscosity and f_k. Current shock position is $x/c \simeq 0.5$. In the plot legend, $f_{k,1}$ and $f_{k,2}$ refer to the estimates of eqs. (6) and (7), respectively.
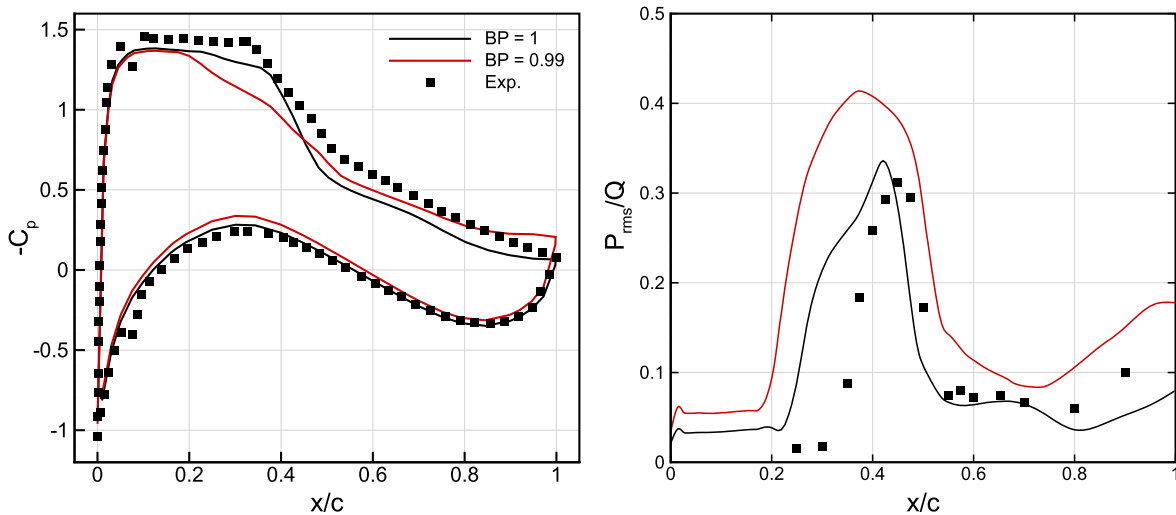

Fig. 7. Pressure coefficient and RMS for different back pressure values.

in the experiments. Overall, very good agreement was found with the experiments.

4.5.5. Buffet dynamics and flow topology

Here, further details on the 3D buffet dynamics are given. The usage of PANS introduced benefits in the prediction of transonic buffet. The URANS simulation converged to a steady state, while PANS was able to predict the buffet. In the former case, the corner separation induced a spanwise flow deviation at the trailing edge that prevented the flow from separating. Even if the flow separated at the shock foot, the separation region did not merge with the one at the trailing edge and the buffet was inhibited. The main reasons can be found in an excessive flow separation at the corner, together with a too high level of eddy viscosity given from the URANS in the post-shock region. Therefore, the presence of the tunnel walls did not help the development of the self-sustained shock oscillation. Conversely, the PANS simulation predicted a buffet flow that develops following a precise pattern. Approaching the most downstream position, the flow is attached and the shock strength increases until the flow separates underneath; at the same time, trailing edge separation occurs due to the reduced eddy viscosity. The two regions merge around the centerline inducing a flow acceleration between the corner and central separated regions. The effect of this is the

creation of a vortical structure at the interface between the attached and separated boundary layer. When the flow is fully separated after the shock, this is affected by the disturbances coming from the trailing edge, and the shock begins to move upstream. In parallel, the aforementioned vortical structures propagate in the separated region and extend to the entire wingspan giving rise to a separated region characterized by large stall cells, in agreement with what was observed in the experiments (see. Fig. 12 (d-e)). This reflects in a non-uniform shock front. Approaching the most upstream position, the shock strength decreases and the flow reattaches completely so that a new period begins with the shock moving downstream.

The strong flow three-dimensionality is confirmed by the numerical schlieren visualizations in Fig. 13. The visualizations were obtained by averaging the density gradient magnitude in the spanwise direction and compared with the experimental images (Fig. 13, bottom plots). At the most downstream position, the shock front is straight for the greater part of the span and slightly deflects near the sidewall. At this condition, the boundary layer is attached. On the other hand, at the most upstream position, there is a large flow separation, and the shock front is not uniform. This is confirmed by the wide region of high density gradient (the predominant component is in the longitudinal direction) in the right plots in Fig. 13.
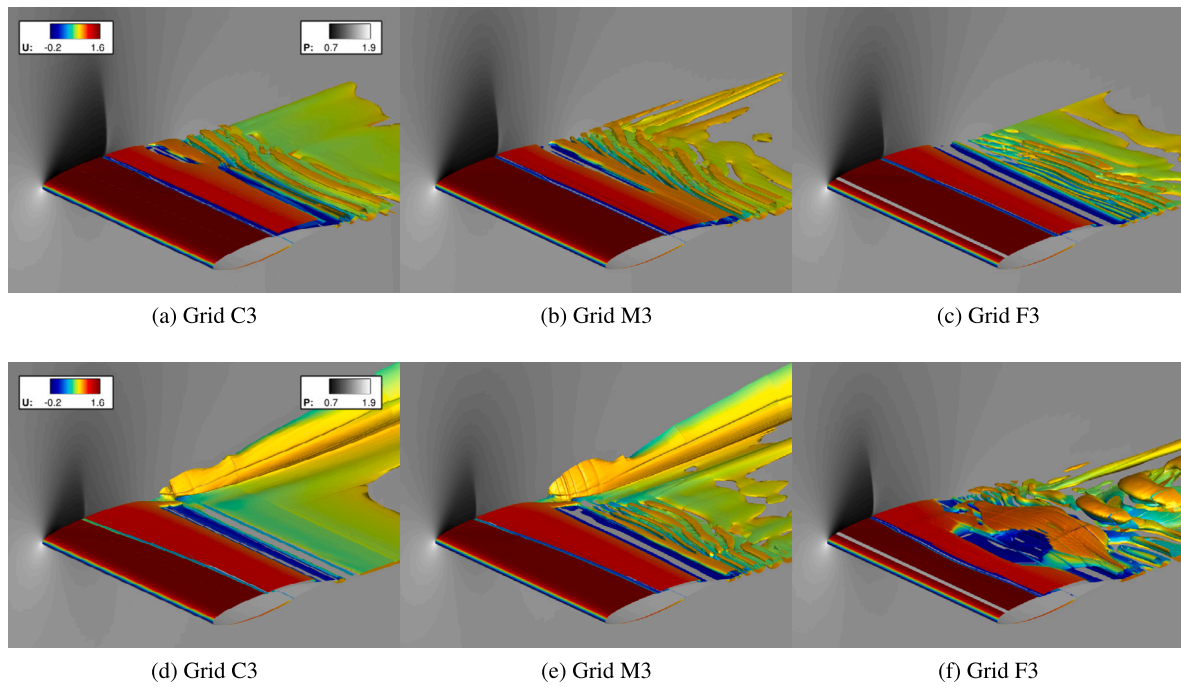
(a) Grid C3   (b) Grid M3   (c) Grid F3

(d) Grid C3   (e) Grid M3   (f) Grid F3

Fig. 8. Iso surfaces of Q-Criterion at $Q = 0.1$ for the confined configuration at different grid sizes. Top: most downstream shock position; bottom: most upstream shock position.
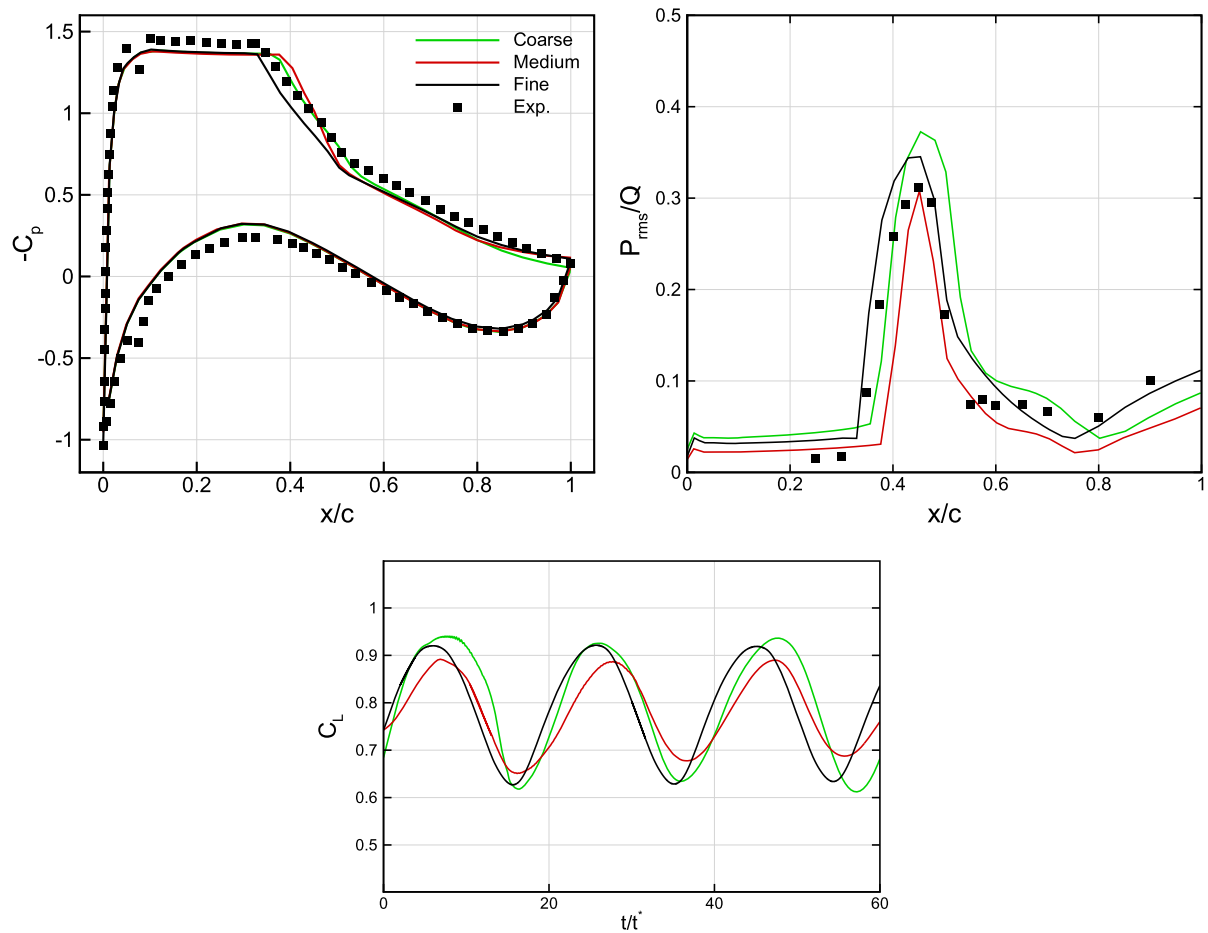

Fig. 9. Top: pressure coefficient (left) and RMS (right) for different grid resolutions; bottom: lift coefficient history.
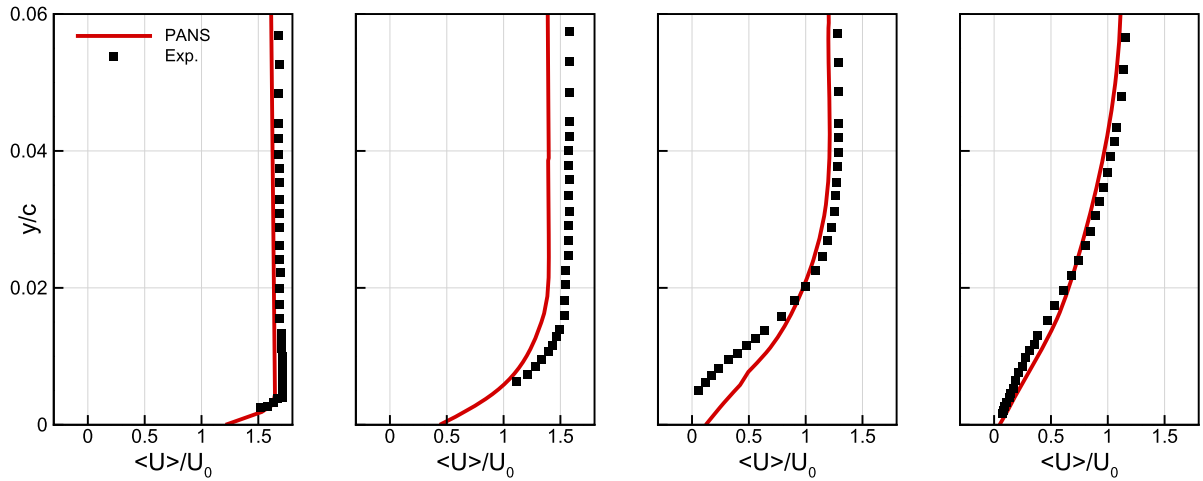
Fig. 10. Mean value profiles of the longitudinal velocity component. From left to right: $x/c = 0.28$, 0.45, 0.6, 0.75.
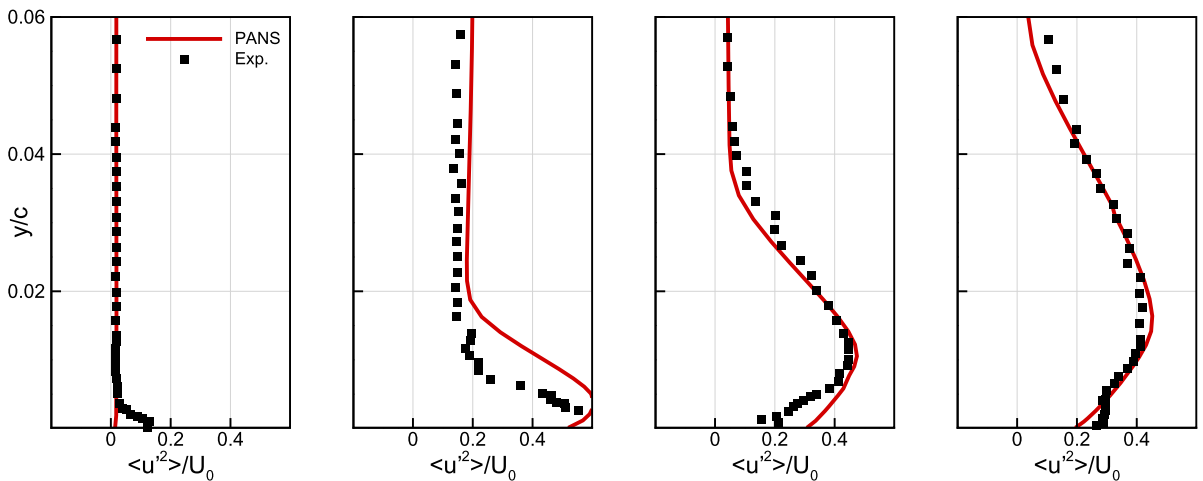

Fig. 11. RMS profiles of the longitudinal velocity component. From left to right: $x/c = 0.28$, 0.45, 0.6, 0.75.

4.5.6. Spectral analysis

Fig. 14 shows the power spectral density (right plot) of the signal pressure at $x/c = 0.45$ and $z/c = 1.6$ (left plot), compared with experiments. The fundamental and secondary frequencies are clearly detected, although a discrepancy with the experiments is present. This is particularly evident looking at the difference in the periods of the pressure signals in the left plot. A slight difference in the mean shock position, shown in Fig. 9, top plots, resulted in a better agreement with the pressure signal at $x/c = 0.43$. It has to be noted that the raw experimental data is not available for processing alongside the CFD, adding to the observed differences.

Fig. 15 shows the power spectral density at different locations around the aerofoil at $z/c = 1.6$. The first three probes were located on the model at $x/c = 0.1$, 0.45 and 0.9, respectively, while the fourth probe located at $x/c = 1.2$ and $y/c = 0.03$. Three mean frequencies are detected: a fundamental buffet frequency around 50-60 Hz (the experimental buffet frequency was 69 Hz) with the secondary harmonics, a bump around 1000-2000 Hz, and another in the wake around 5000-6000 Hz. This subdivision is coherent with the analysis of Szubert et al. [41] that associates these three values to the buffet motion, Von Karman shedding and Kelvin-Helmholtz instabilities, respectively. While the fundamental and secondary harmonics were detected by every probe, just the last two ones were able to capture the presence of other types of instability.

The dependence of the PSD on the streamwise and spanwise coordinate was studied using sound pressure levels, defined as

$$\text{SPL} = 20 \, \text{Log} \left(\frac{\text{PSD}}{2 \times 10^{-5}} \right), \tag{20}$$

coherently with the paper of Jacquin et al. [1]. Figs. 16 and 17 show the distribution of SPL along the streamwise and spanwise directions, respectively. Fig. 16 clearly shows the buffet frequency and the secondary harmonics all over the chord. The energy content associated with the pressure signals within the region of shock motion is higher than at other locations because of the higher level of fluctuations.

Fig. 17 shows that the energy distribution between frequencies is invariant in the spanwise direction, in spite of the 3D flow topology developed over the buffet period. The same behaviour was shown in the work of Jacquin et al. [1].

4.6. Computational performance and cost

Table 3 presents the CPU cost of the PANS and URANS simulations. The comparison was done over one characteristic travel time, i.e. over 100 computational timesteps. In the analysis, the same grid and the same number of processors were used. Since the URANS tends to a steady solution while the PANS describes an intrinsically unsteady flow, the number of inner iterations required to meet the convergence crite-
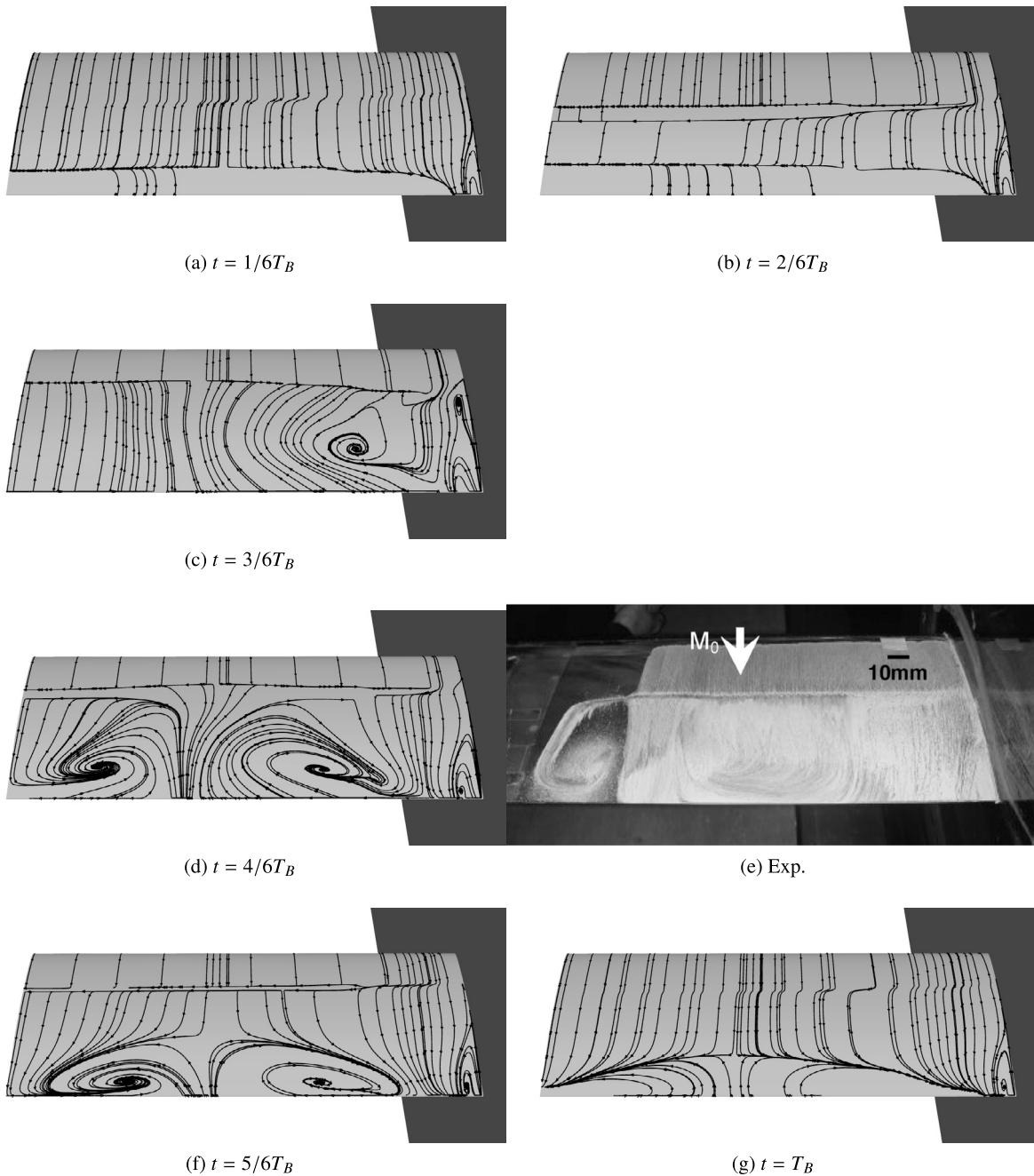
(a) $t = 1/6 T_B$

(b) $t = 2/6 T_B$

(c) $t = 3/6 T_B$

(d) $t = 4/6 T_B$

(e) Exp.

(f) $t = 5/6 T_B$

(g) $t = T_B$

Fig. 12. Surface friction lines at different phases of the buffet period T_B. The experimental oil flow visualization was introduced for comparison purposes.

Table 3

Comparison between computational times of PANS and URANS. ABAH: apply boundary and halo; IATS: initialize and time step; CHOG: calculate high order gradients; CRJ: calculate residual Jacobian; CP: calculate preconditioner; SLS: solve linear system.

	GCG iter.	ABAH [s]	IATS [s]	CHOG [s]	CRJ [s]	CP [s]	SLS [s]	Tot
URANS	3.86	0.31	0.055	0.00024	0.65	0.09	0.83	**1.95**
PANS	4.59	0.31 (+1%)	0.055 (-1%)	0.00025 (+8%)	0.70 (+7%)	0.09 (-3%)	0.85 (+2%)	**2.00 (+3.1%)**

rion on the flow residual is different; therefore, the averages were taken over the number of inner iterations of the implicit dual-time stepping scheme. This was done to identify the net additional cost of the PANS routine in the solver. From the table, it can be seen that the higher increase is that on the evaluation of the residual Jacobian, where the PANS routine is recalled to modify the source terms in the k and ω equations. Moreover, the number of iterations of the GCG scheme for the solution of the linear scheme is slightly increased. This reflects in an increase in the total computational time of about 3% when compared to URANS.

This shows the capability of PANS to work in URANS-mode, helping unlock flow unsteadiness by lowering the eddy viscosity in regions of high turbulent content, and in agreement with the grid resolution.
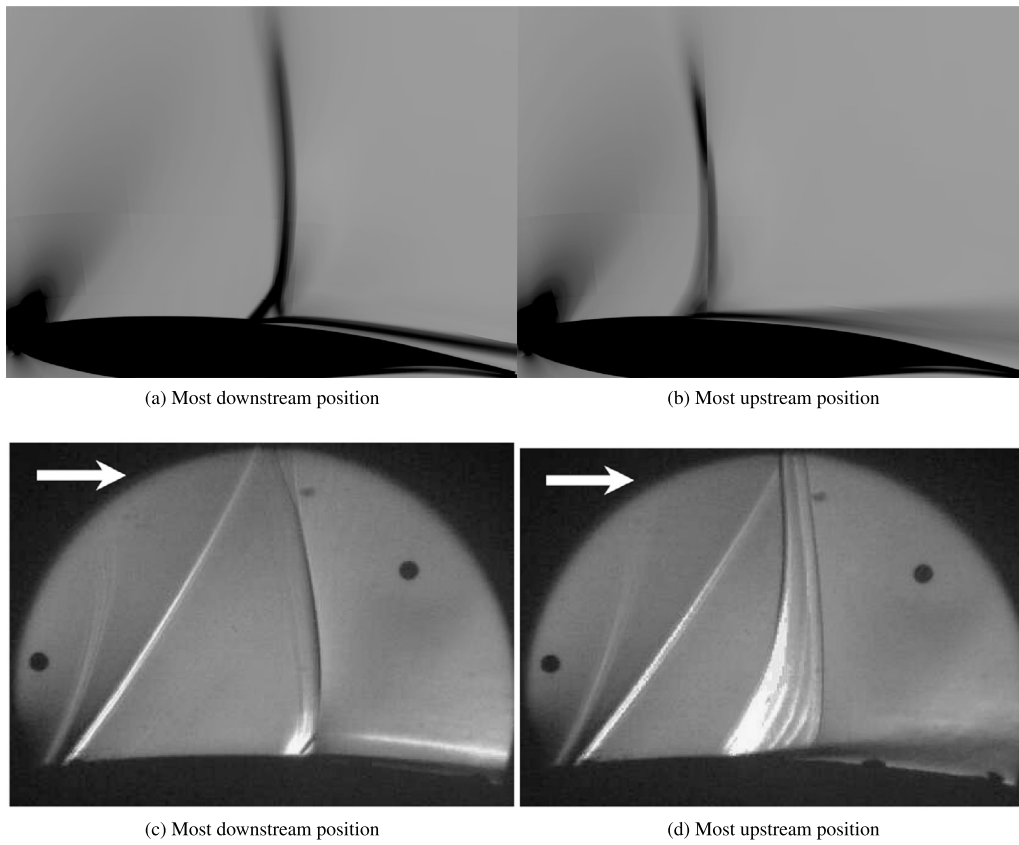
(a) Most downstream position

(b) Most upstream position

(c) Most downstream position

(d) Most upstream position

Fig. 13. Numerical (top) and experimental (bottom) schlieren visualizations. The visualizations were obtained by averaging the density gradient magnitude in the spanwise direction. Pictures of the experiments taken from [1].
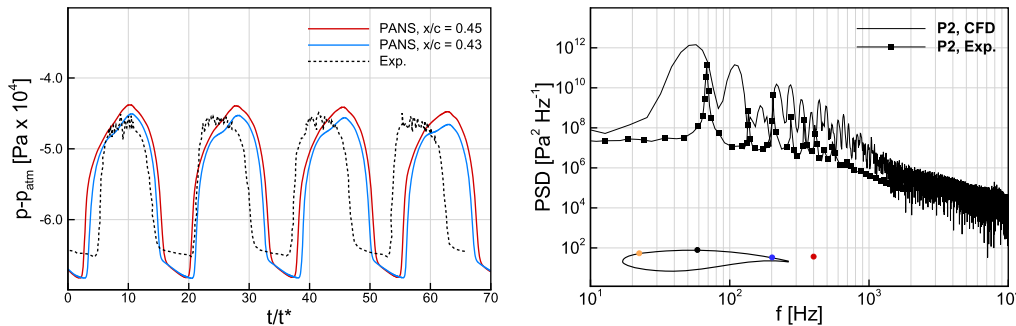

Fig. 14. Pressure signal (left) and power spectral density (right) at $x/c = 0.45$ and $z/c = 1.6$. In the left plot, the pressure signal at $x/c = 0.43$ was also plotted.
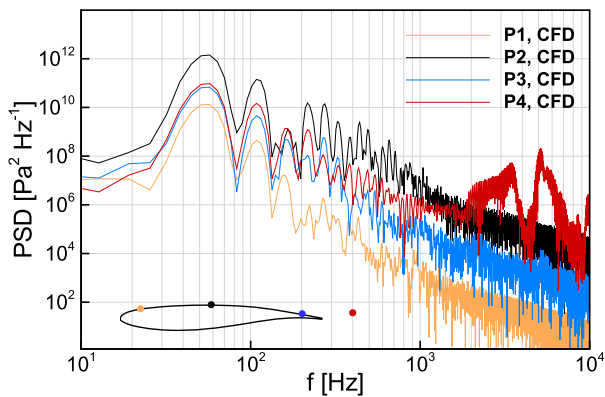

Fig. 15. Power spectral density of the pressure at different points in the domain. The position with respect to the aerofoil is indicated in the bottom left sketch.

5. Conclusions

In this work, the application of PANS for the flow around the OAT15A section at high Reynolds number was presented. Computations on both confined and unconfined configurations were carried out. The wind tunnel walls were accounted and symmetry boundary conditions at the symmetry plane of the wind tunnel were imposed. The wind tunnel presence influenced the buffet dynamics by introducing a strong three-dimensionality to the flow. At pre-buffet conditions, the shock was influenced by the presence of the wind tunnel and displayed a front bending when approaching the wall. The PANS approach used in this work recovered the URANS behaviour, provided a reasonable distribution of the f_k parameter.

After the onset, although the buffet mechanism maintained its two-dimensional nature, the interaction with the separated region at the wall-wing junction was shown to be crucial in the generation of large 3D vortical structures on the wing. This was not shown in the majority
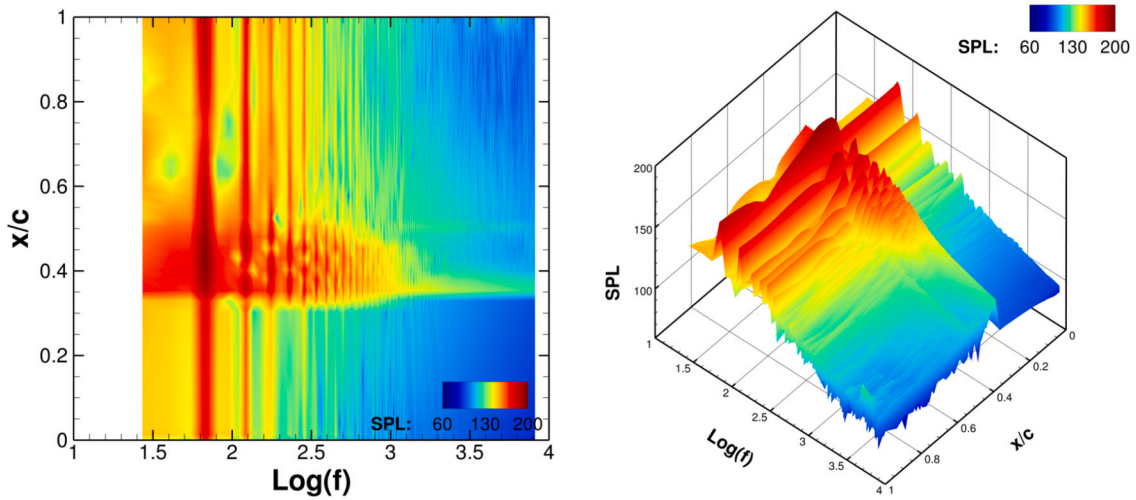
Fig. 16. Sound pressure levels along the chord on the upper surface at $z/c = 1.6$. Left: 2D representation; right: 3D representation.
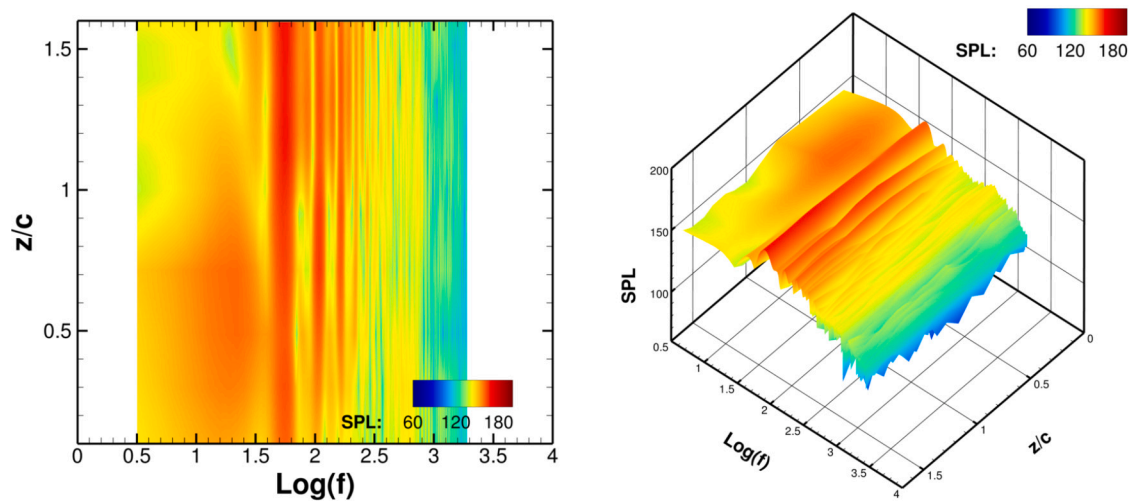

Fig. 17. Sound pressure levels along the span on the upper surface at $x/c = 0.6$. Left: 2D representation; right: 3D representation.

of the published works, where a typical 2D behaviour with an alternated separation and reattachment of the flow on the suction side of the airfoil was shown. For both configurations, URANS simulations were not able to predict the buffet, even at an angle of attack well beyond the buffet onset, while the use of PANS unlocked the shock oscillations. The flow physics is captured correctly, as confirmed by comparison with the experiments in Figs. 9 to 13, with the unsteady loads exhibiting periodic oscillations.

Because of the lack of detailed documentation for the experimental settings, some preliminary study was required to find the correct setup to obtain the correct mean shock position. The f_k parameter was clipped to a value of 0.6 to avoid an excessive reduction of the eddy viscosity, considering the spatiotemporal discretization adopted. Moreover, the back pressure value revealed highly impactful on the CFD prediction. A lower value of this quantity resulted in large SIO and a pressure gap on both sides of the aerofoil. Therefore, no definitive conclusions can be drawn in the absence of the correct setup. The PANS approach proved to be able to work at different grid resolutions. In comparison with URANS, a little additional expense ($\simeq 3\%$) was introduced by the PANS routine. This latter revealed beneficial in describing the self-sustained oscillation even with a coarse, RANS-like grid and allowed for scale-resolving when a finer grid was used. In the latter, the description of the buffet dynamics was more accurate since the detection of stall cells on the upper surface of the wing was enabled.

The presence of stall cells was recently observed on configurations with high aspect ratio (see the works of Plante et al. [48] and He and Timme [51]), and on a different test case with wind tunnel [50]. The evolution of the separated region suggests that pressure disturbances originated at the wing-wall junction and propagated towards the centre of the wind-tunnel, confirming the results of the stability analysis of Sansica et al. [50]. On that basis, one can speculate that this case is intermediate between common 2D cases, with stall cells developing periodically over the span, and 3D cases with buffet cells propagating in the outboard direction.

Future efforts will be devoted to the application of this technique for different flows with SBLI. Moreover, the estimate of f_k will be improved to allow for a more automatic clipping according to grid size and local turbulence content to avoid any preliminary calibration. The use of PANS in conjunction with a non-linear correction of the Reynolds stress and a 3-equation model will be considered to improve the performance of this approach in dealing with corner and transitional flows, respectively.

CRediT authorship contribution statement

Andrea Petrocchi: Data curation, Software, Validation, Writing – original draft. **George Barakos:** Conceptualization, Software, Supervision, Writing – original draft, Writing – review & editing.

Table A.4

Overview of computations for the OAT15A 2D configuration with different closure models. SA: Spalart-Allmaras; BSL: baseline k-ω; SST: Menter's Shear Stress Model; KKL: $k - kL$ model; SALSA: Spalart–Allmaras with strain-adaptive formulation; LEA: Linearized Explicit Algebraic k-ω; EHRSM: ϵ^h-Reynolds stress model; EDW: Edwards-Chandra modification of SA; KWW: Wilcox's k-ω; CC: compressibility correction; RC: rotation correction; SORSM: stress-Omega RSM; EARSM: Explicit Algebraic Reynolds Stress Model.

First Author	Year	Solver	Model	Buffet	St	ΔC_L
Deck [40]	2005	FLU3M	SA	no SIO		
Thiery & Coustols [37]	2006	elsA	SA	no SIO		
			BSL	no SIO		
			KKL	SIO	$0.0679 \div 0.0743$	$\simeq 0.22$
			SST	SIO	$0.0679 \div 0.0743$	$\simeq 0.14$
Huang [42]	2012	UNITs	SST	no SIO		
Illi et al. [36]	2012	TAU	SA	no SIO		
			SALSA	SIO	$0.0708 \div 0.0727$	$0.10 \div 0.16$
			SST	no SIO		
			LEA	no SIO		
			EHRSM	SIO	$\simeq 0.066$	$\simeq 0.30$
Grossi et al. [35]	2014	NSMB	SA	no SIO		
			SA+CC	no SIO		
			SST	no SIO		
			EDW	SIO		
			EDW+CC	SIO	0.070	$\simeq 0.30$
			SALSA	SIO		
			KWW	SIO		
Sartor et al. [73]	2015	elsA	SA	SIO	0.0737	$\simeq 0.06$
Tian [74]	2017	-	SA	SIO		
Giannelis et al. [75]	2018	ANSYS Fluent	SA-RC	no SIO		
			SST	no SIO		
			SST-mod[a]	SIO	0.0691	0.16
			SORSM	SIO	0.0713	0.33
Zimmernann [76]	2018	FLOWer	SALSA	SIO	$0.0665 \div 0.0694$	
		TAU	SALSA	SIO	$0.0669 \div 0.0698$	
Plante & Laurendeau [77]	2019	NSCODE	SA	no SIO		
			SA+CC	SIO	0.0698	$\simeq 0.27$
			EDW	no SIO		
			EDW+C	SIO	0.0698	$\simeq 0.30$
Zhao et al. [78]	2020	-	SA	SIO	0.0717	
			SST	SIO[b]		
			EARSM	no SIO		
Petrocchi & Barakos [70]	2023	HMB3	SST	no SIO		

[a] A reduction of the a_1 coefficient of the SST model was applied.
[b] Very mild oscillations were detected.

Declaration of competing interest

The authors declare the following financial interests/personal relationships which may be considered as potential competing interests: Andrea Petrocchi was supported by the European Union.

Data availability

Data will be made available on request.

Appendix A. Past OAT15A simulation using URANS

This appendix provides an overview of CFD computations using URANS for the OAT15A aerofoil at $\mathrm{Re}_c = 3 \times 10^6$, $\mathrm{M}_\infty = 0.73$ and $\alpha = 3.5$ deg. This test case at the reported flow conditions was widely investigate because of the availability of experimental data. Therefore, it was used to validate the ability of different turbulence models and CFD solvers to predict buffet.

Table A.4 is a collection of CFD works using a wide variety of solvers (column 3) and turbulence models (column 4). In the last column, the ability to predict shock-induced oscillations (SIO: yes; no SIO: no) is reported. The results show a big scatter in the prediction of the main quantities of interest, i.e. buffet frequency, amplitude of oscillations, mean and RMS pressure distribution. As the results for the aforementioned works were not consistently reported in the cited works, they were not included in the table. Also, works providing results with the same setup (CFD solver, turbulence model, grid, timestep) of one of those in the table were not mentioned to avoid redundancy.

Appendix B. Literature on PANS works

The PANS approach was used with increasing frequence over the years. Table B.5 is a collection of works solving PANS equations to give the readers an idea of the increased popularity of the approach over the years. While in principle the method was only tested on canonical configuration, mostly using a *constant* approach for f_k estimate, more sophisticated estimates were developed, extending the use of PANS to various applications.

Appendix C. Effect of transition location and f_k clip

C.1. Transition to turbulence

Here the role of the laminar-to-turbulent transition of the boundary layer is investigated. The position of the tripping device was indicated in the experimental references, but no characterisation of the transition to turbulence was given. Therefore, there is uncertainty around

Table B.5

List of PANS computations found in literature. S: static approach; D: dynamic approach.

Authors	Year	Test case	Re	M_∞	Model
Constant					
Girimaji et al. [2,79,80]	2005-2006	Turb. Square Jet	1.84×10^5	-	k-ϵ
Lakshimpathyi & Girimaji [8]	2006 [8], 2010 [81]	Circular Cylinder	1.4×10^4	-	k-ϵ
	2010	Circular Cylinder	1.4×10^4	-	k-ϵ
Frendi et al. [13]	2007	Backward-facing step	3.75×10^4	-	k-ϵ
Gerolymos & Vallet [82]	2007	Rod/Airfoil	4.7×10^4	0.21	RSM
Jeong & Girimaji [11]	2010	Square Cylinder	2.2×10^4	-	k-ϵ
Huang & Wang [83]	2011	Hydrofoil with cavitation	7×10^5	-	k-ϵ
Ma et al. [15,16]	2011	Hill flow	3.7×10^4	-	k-ϵ/LR-k-ϵ
		Channel flow	9.5×10^2	-	
		Curved Duct	9.5×10^2	-	
Srinivasan & Girimaji [84]	2014	Jet in cross stream	5.3×10^6	-	k-ω SST
Roy et al. [85]	2015	Lid-driven Cavity	1×10^4	-	k-ω
Pereira et al.	2015 [86], 2018 [9]	Circular Cylinder	3.9×10^3	-	k-ω SST
Bonnifet et al. [21]	2017	OAT15A	3×10^6	0.73	RSM-GLVY
Klapwijk et al.	2019 [23,87],2020 [88]	Channel flow	$180 \div 395$	-	k-ω SST
Saroha et al.	2020 [89]	Heated Sphere	1×10^4	-	NL k-ϵ
	2020 [90]	Heated Cylinder	2.14×10^4	-	
Dzanic et al. [91]	2022	Periodic hill	1.0595×10^4	-	k-ω SST
		Circular cylinder	3.9×10^3	-	
Static					
Elmiligui et al. [7]	2004	Circular Cylinder	5×10^4	0.3	k-ϵ
Abdol-Hamid & Girimaji [6]	2004	Circular Cylinder	5×10^4	0.3	k-ϵ
Song & Park [10]	2009	Square Cylinder	2.14×10^4	-	k-ω
Foroutan & Yavuzkurt [92]	2014	Swirling jet	3×10^4	-	LR-k-ϵ
Dynamic					
Basu et al. [19]	2007	Cavity	0.6×10^6/ft	1.19	k-ϵ
Basara et al.	2011 [14]	Turbulent Channel	6.5×10^2	-	k-ϵ-ξ-f
	2015 [24]	Wall-mounted Cube	1.3×10^4	-	
	2018 [12]	Square Cylinder	2.14×10^4	-	
Krajnovic et al.	2012 [25]	Landing Gear	1×10^6	-	k-ϵ-ξ-f
	2015 [26]	Bluff body	4.0×10^4	-	
	2016 [93]	Simplified Vehicle	9.0×10^5	-	
Han et al. [94]	2013	Bluff body	3.0×10^4	-	k-ϵ-ξ-f
Luo et al. [20]	2015	Circular Cylinder	4.5×10^7	2.46	k-ω SST
		Ramped Cavity	4.5×10^7	2.92	
Mirzaei et al. [95]	2015	Bluff body	3.0×10^4	-	k-ϵ-ξ-f
Minelli et al.	2017 [96]	Simplified Track Cabin	5.0×10^5	-	k-ϵ-ξ-f
	2018 [27]	Oscillating Track Cabin	5.0×10^5	-	
Zhang et al. [28]	2018	Ship	8.0×10^4	-	k-ϵ-ξ-f
Luo [3]	2019	Backward-facing Step	5.1×10^3	-	k-ω SST
Davidson & Friess	2019 [17], 2020 [18]	Channel flow	5.2×10^3	-	LR-k-ϵ
		Hump flow	9.36×10^5	-	
		Hill flow	1.06×10^4	-	
Liu et al. [29]	2022	Rotating Channel Flow	7000	-	k-ω SST
		Centrifugal pump	5.5×10^4	-	
Moosavifard et al. [97]	2022	Circular Cylinder	4.8×10^4	0.21	k-ϵ-ξ-f
Nastac & Frendi [98]	2022	Supersonic retropropulsion	5.0×10^6	4.61	k-ω SST
Wang et al. [30]	2023	Square-back Van	2.5×10^5	-	k-ϵ-ξ-f

the location of the actual transition point. Therefore, the scope of this study is to assess whether imposing transition at the experimental location leads to the right prediction, other than providing a comparison with the fully turbulent case. The transition was fixed by imposing $\mu_T/\mu = 0$ at different streamwise locations, i.e. $x/c = 0.07, 0.25$, and the results were compared with the fully turbulent case. The first value selected corresponds to the actual location of the tripping device in the experiments, while the second was chosen to account for eventual delays in the boundary layer transition to turbulence. Fig. C.18 shows the streamwise velocity component on the upper surface over time for the three cases. The separation line is represented by the solid, black line. Although the average shock position moves downstream with a later transition, when the transition is set to $x/c = 0.25$, a second separated flow region arises in the laminar part of the boundary layer close to the leading edge of the aerofoil. This reflects in a higher value of the pressure RMS in the first part of the aerofoil with respect to the other cases

(see Fig. C.18, right plot) and a lower value of the C_p on the suction side (see Fig. C.18, left plot).

The results are in agreement with the study of Garbaruk et al. [99], who observed an increase in lift associated with the downstream shock motion by delaying the transition on the suction side of the aerofoil. On the other hand, the transition location on the aerofoil pressure side has negligible effects on the mean quantities. (See Fig. C.19.)

C.2. Value of f_k clip

Here the effect of the inferior clip of the parameter f_k is studied for different angles of attack. This value is strongly related to the mesh resolution. Indeed, without clipping f_k, the risk of too low eddy viscosity in some regions of the flow field is high, especially for coarse grids. Fig. C.20 shows the pressure coefficient and RMS for two different values of $f_{k,\text{inf}}$. A too low value of the clip, 0.4 in this case, results in a too upstream shock position with respect to the experiments. The low

(a) Fully turbulent
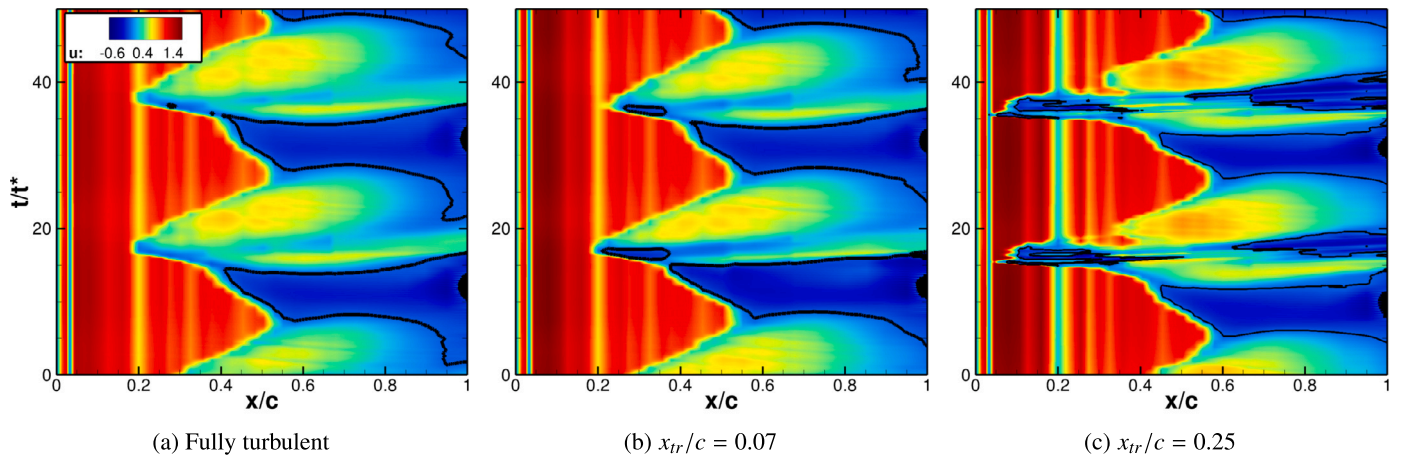
(b) $x_{tr}/c = 0.07$

(c) $x_{tr}/c = 0.25$

Fig. C.18. Temporal evolution of the streamwise velocity component on the upper surface of the aerofoil at $z/c = 1.6$ for different transition locations. The solid, black line represents $U/U_0 = -0.001$ isoline.
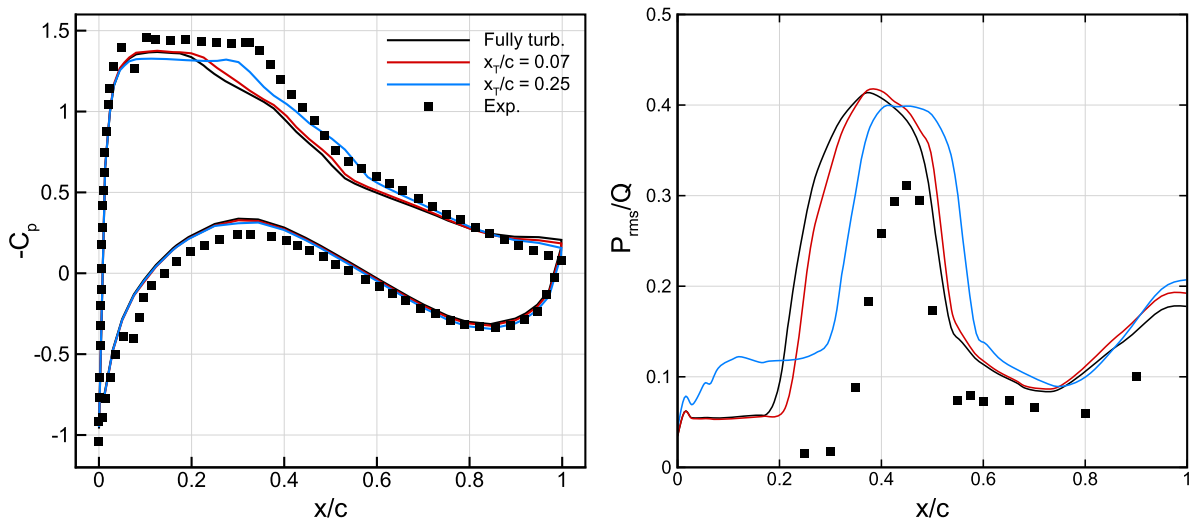

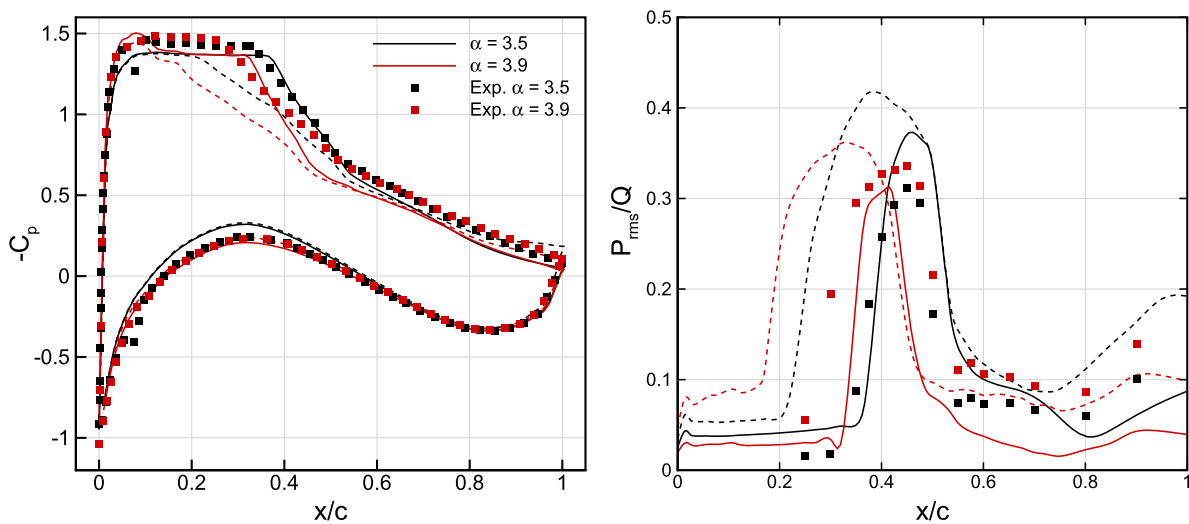**Fig. C.19.** Pressure coefficient and RMS for different transition locations.

Fig. C.20. Pressure coefficient and RMS for different angles of attack and clip of f_k. Dotted lines: $f_{k,min} = 0.4$; solid lines: $f_{k,min} = 0.6$.

level of eddy viscosity promotes boundary layer separation and raises the level of flow unsteadiness at the TE. With the current mesh resolution, this level of eddy viscosity causes a wrong prediction of the global flow features. Conversely, adopting the higher value of 0.6, the prediction is improved, at both angles of attack. The comparison is, overall, good for both angles of attack.

References

[1] L. Jacquin, P. Molton, S. Deck, B. Maury, D. Soulevant, Experimental study of shock oscillation over a transonic supercritical profile, AIAA J. 47 (2009) 1985–1994, https://doi.org/10.2514/1.30190.

[2] S. Girimaji, K. Abdol-Hamid, Partially-averaged Navier Stokes model for turbulence: implementation and validation, in: AIAA Aerospace Sciences Meeting and Exhibit, Reno, NE, USA, 2005.

[3] D. Luo, RNumerical simulation of turbulent flow over a backward facing step using partially averaged Navier-Stokes method, J. Mech. Sci. Technol. 33 (2019) 2137–2148, https://doi.org/10.1007/s12206-019-0416-9.

[4] P. Spalart, W. Jou, M. Strelets, S. Allmaras, Comments on the feasibility of les for wings, and on a hybrid rans/les approach, in: Advances in DNS/LES: Direct Numerical Simulation and Large Eddy Simulation, Reno, NV, USA, 1997.

[5] P. Spalart, C. Streett, Young-Person's Guide to Detached-Eddy Simulation Grids, Tech. Rep., nASA/CR-2001-211032, National Aeronautics and Space Administration, 2001.

[6] K. Abdol-Hamid, S. Girimaji, A Two-Stage Procedure Toward the Efficient Implementation of PANS and Other Hybrid Turbulence Models, Tech. Rep., nASA/TM-2004-213260, National Aeronautics and Space Administration, 2004.

[7] A. Elmiligui, K. Abdol-Hamid, S. Massey, S.P. Pao, Numerical study of flow past a circular cylinder using RANS, hybrid RANS/LES and PANS formulations, in: 22nd Applied Aerodynamics Conference and Exhibit, Providence, Rhode Island, 2004.

[8] S. Lakshmipathy, S. Girimaji, Partially-averaged Navier Stokes method for turbulent flows: $k - \omega$ model implementation, in: AIAA Aerospace Sciences Meeting and Exhibit, Reno, NE, USA, 2006.

[9] F. Pereira, G. Vaz, L. Eca, S. Girimaji, Simulation of the flow around a circular cylinder at Re = 3900 with partially-averaged Navier-Stokes equations, Int. J. Heat Fluid Flow 69 (2018) 234–246.

[10] C.-S. Song, S.-O. Park, Numerical simulation of flow past a square cylinder using partially-averaged Navier–Stokes model, J. Wind Eng. Ind. Aerodyn. 97 (2009) 37–47, https://doi.org/10.1016/j.jweia.2008.11.004.

[11] E. Jeong, S. Girimaji, Partially averaged Navier-Stokes (PANS) method for turbulence simulations-flow past a square cylinder, J. Fluids Eng. 132 (2010) 1–11, https://doi.org/10.1115/1.4003153.

[12] B. Basara, Z. Pavlovic, S. Girimaji, A new approach for the calculation of the cutoff resolution parameter in bridging methods for turbulent flow simulation, Int. J. Heat Fluid Flow 74 (2018) 76–88, https://doi.org/10.1016/j.ijheatfluidflow.2018.09.011.

[13] A. Frendi, A. Tosh, S. Girimaji, Flow past a backward-facing step: comparison of PANS, DES and URANS results with experiments, Int. J. Comput. Methods Eng. Sci. Mech. 8 (2007) 23–38, https://doi.org/10.1080/15502280601006207.

[14] B. Basara, S. Krajnovic, S. Girimaji, Z. Pavlovic, Near-wall formulation of the partially averaged Navier–Stokes turbulence model-layer interaction, AIAA J. 49 (2011) 2627–2636, https://doi.org/10.2514/1.J050967.

[15] J.-M. Ma, F.-J. Wang, X. Yu, Z.-Q. Liu, A partially-averaged Navier-Stokes model for hill and curved duct flow, J. Hydrodyn. 23 (2011) 466–475, https://doi.org/10.1016/S1001-6058(10)60137-0.

[16] J.-M. Ma, S.-H. Peng, L. Davidson, F. Wang, A low Reynolds number variant of partially-averaged Navier–Stokes model for turbulence, Int. J. Heat Fluid Flow 32 (2011) 652–669, https://doi.org/10.1016/j.ijheatfluidflow.2011.02.001.

[17] L. Davidson, C. Friess, A new formulation of f_k for the PANS model, J. Turbul. 20 (5) (2019) 322–336, https://doi.org/10.1080/14685248.2019.1641605.

[18] C. Friess, L. Davidson, A formulation of PANS capable of mimicking IDDES, Int. J. Heat Fluid Flow 86 (2020) 1–25, https://doi.org/10.1016/j.ijheatfluidflow.2020.108666.

[19] D. Basu, A. Hamed, K. Dias, Assessment of partially averaged Navier/Stokes (PANS) multiscale model in transonic turbulent separated flows, in: ASME/AJME 2007 5th Joint Fluids Engineering Conference, San Diego, CA, USA, 2007.

[20] D. Luo, C. Yan, X. Wang, Computational study of supersonic turbulent-separated flows using partially averaged Navier-Stokes method, Acta Astronaut. 107 (2015) 234–246, https://doi.org/10.1016/j.actaastro.2014.11.029.

[21] V. Bonnifet, G. Gerolymos, I. Vallet, Transonic buffet prediction using partially averaged Navier-Stokes, in: 23rd AIAA Computational Fluid Dynamics Conference, Denver, Colorado, USA, 2017.

[22] F. Menter, Two-equation eddy-viscosity turbulence models for engineering applications, AIAA J. 32 (1994) 1598–1605, https://doi.org/10.2514/3.121495.

[23] M. Klapwijk, T. Lloyd, G. Vaz, O.V. Terwisga, P.A.N.S. Simulations, Low versus high Reynolds number approach, in: VIII International Conference on Computational Methods in Marine Engineering, Goteborg, Sweden, 2019.

[24] B. Basara, Fluid flow and conjugate heat transfer in a matrix of surface-mounted cubes: a PANS study, Int. J. Heat Fluid Flow 51 (2015) 166–174, https://doi.org/10.1016/j.ijheatfluidflow.2014.10.012.

[25] S. Krajnovic, R. Larusson, B. Basara, Superiority of PANS compared to LES in predicting a rudimentary landing gear flow with affordable meshes, Int. J. Heat Fluid Flow 37 (2012) 109–122, https://doi.org/10.1016/j.ijheatfluidflow.2012.04.013.

[26] S. Krajnovic, G. Minelli, B. Basara, Partially-averaged Navier–Stokes simulations of two bluff body flowsn, Appl. Comput. Math. (2015), https://doi.org/10.1016/j.amc.2015.03.136.

[27] G. Minelli, S. Krajnovic, B. Basara, A flow control study of a simplified, oscillating truck cabin using PANS, J. Fluids Eng. 140 (2018) 121101, https://doi.org/10.1115/1.4040225.

[28] J. Zhang, G. Minelli, A. Rao, B. Basara, R. Bensow, S. Krajnovic, Comparison of PANS and LES of the flow past a generic ship, Ocean Eng. 165 (2018) 221–236, https://doi.org/10.1016/j.oceaneng.2018.07.02333.

[29] B. Liu, W. Yang, Z. Liu, A PANS method based on rotation-corrected energy spectrum for efficient simulation of rotating flow, Frontiers in Energy Research 10 (2022) 894258, https://doi.org/10.3389/fenrg.2022.894258.

[30] J. Wang, G. Minelli, G. Cafiero, G. Iuso, K. He, B. Basara, G. Gao, S. Krajnovic, Validation of PANS and effects of ground and wheel motion on the aerodynamic behaviours of a square-back vani, J. Fluid Mech. 958 (2023) A47, https://doi.org/10.1017/jfm.2023.47.

[31] B. Lee, Self-sustained shock oscillations on airfoils at transonic speeds, Prog. Aerosp. Sci. 37 (2001) 147–196, https://doi.org/10.1016/S0376-0421(01)00003-3.

[32] N. Giannelis, G. Vio, O. Levinski, A review of recent developments in the understanding of transonic shock buffet, Prog. Aerosp. Sci. 92 (2017) 39–84, https://doi.org/10.1016/j.paerosci.2017.05.004.

[33] G. Barakos, D. Drikakis, Numerical simulation of transonic buffet fow using various turbulence closures, Int. J. Heat Fluid Flow 21 (2000) 620–626, https://doi.org/10.1016/S0142-727X(00)00053-9.

[34] E. Goncalves, R. Houdeville, Turbulence model and numerical scheme assessment for buffet computations, Int. J. Numer. Methods Fluids 46 (2004) 1127–1152, https://doi.org/10.1002/d.777.

[35] F. Grossi, M. Braza, Y. Hoarau, Prediction of transonic buffet by delayed detached-eddy simulation, AIAA J. 52 (2014) 2300–2312, https://doi.org/10.2514/1.J052873.

[36] S. Illi, T. Lutz, E. Kramer, On the capability of unsteady RANS to predict transonic buffet, in: Proceeding of the Third Symposium Simulation of Wing and Nacelle Stall, Braunschweig, Germany, 2012.

[37] M. Thiery, E. Coustols, Numerical prediction of shock induced oscillations over a 2D airfoil: influence of turbulence modelling and test section walls, Int. J. Heat Fluid Flow 27 (2006) 661–670, https://doi.org/10.1016/j.ijheatfluidflow.2006.02.013.

[38] M. Strelets, Detached eddy simulation of massively separated flows, in: 39th Aerospace Sciences Meeting and Exhibit, Reno, NV, USA, 2001.

[39] P. Spalart, S. Deck, M. Shur, K. Squires, M. Strelets, A. Travin, A new version of detached-eddy simulation, resistant to ambiguous grid densities, Theor. Comput. Fluid Dyn. 20 (2006) 181–195, https://doi.org/10.1016/j.ijheatfluidflow.2008.07.001.

[40] S. Deck, Numerical simulation of transonic buffet over a supercritical airfoil, AIAA J. 43 (2005) 1556–1566, https://doi.org/10.2514/1.9885.

[41] D. Szubert, F. Grossi, A. Garcia, Y. Hoarau, J. Hunt, M. Braza, Shock-vortex shear-layer interaction in the transonic flow around a supercritical airfoil at high Reynols number in buffet conditions, J. Fluids Struct. 55 (2020) 276–302, https://doi.org/10.1016/j.jfluidstructs.2015.03.005.

[42] J. Huang, Z. Xiao, J. Liu, S. Fu, Simulation of shock wave buffet and its suppression on an OAT15A supercritical airfoil by IDDES, Sci. China, Phys. Mech. Astron. 55 (2012) 260–271, https://doi.org/10.1007/s11433-011-4601-9.

[43] V. Brunet, S. Deck, Zonal-detached eddy simulation of transonic buffet on a civil aircraft type configuration, in: 38th Fluid Dynamics Conference and Exhibit, Seattle, WA, USA, 2008.

[44] L. Masini, A. Peace, S. Timme, Scale-resolving simulation of shock buffet onset physics on a civil aircraft wing, in: Royal Aeronautical Society 2018 Applied Aerodynamics Conference, Bristol, United Kingdom, 2018.

[45] L. Masini, S. Timme, A.J. Pace, Scale-resolving simulations of a civil aircraft wing transonic shock-buffet experiment, AIAA J. 58 (2020) 4322–4338, https://doi.org/10.2514/1.J059219.

[46] A. Garbaruk, M. Shur, M. Strelets, P.R. Spalart, Numerical study of wind-tunnel walls effects on transonic airfoil flow, AIAA J. 44 (2003) 1046–1054, https://doi.org/10.1016/j.compfluid.2016.03.03.

[47] M. Iovnovich, D.E. Raveh, Numerical study of shock buffet on three-dimensional wings, AIAA J. 53 (2015) 449–463, https://doi.org/10.2514/1.J053201.

[48] F. Plante, J. Dandois, E. Laurendeau, Similarities between cellular patterns occurring in transonic buffet and subsonic stall, AIAA J. 58 (2020) 71–84, https://doi.org/10.2514/1.J058555.

[49] Y. Sugioka, T. Kouchi, S. Koike, Experimental comparison of shock buffet on unswept and 10-deg swept wings, Exp. Fluids 632 (2022) 132, https://doi.org/10.1007/s00348-022-03482-x.

[50] A. Sansica, A. Hashimoto, S. Koike, T. Kouchi, Side-wall effects on the global stability of swept and unswept supercritical wings at buffet conditions, in: AIAA SciTech 2022 Forum, San Diego, CA, USA & Online, 2022.

[51] W. He, S. Timme, Triglobal shock buffet instability study on infinite wings, in: AIAA SciTech Forum 2020, Orlando, FL, USA, 2020.

[52] E. Garnier, S. Deck, Large-eddy simulation of transonic buffet over a supercritical airfoil, in: Direct and Large-Eddy Simulation VII, in: ERCOFTAC Series, vol. 13, 2010, pp. 549–554.

[53] J. Dandois, I. Mary, V. Brion, Large-eddy simulation of laminar transonic buffet, J. Fluid Mech. 850 (2018) 156–178, https://doi.org/10.1063/1.4937426.

[54] Y. Fukushima, S. Kawai, Wall-modeled large-eddy simulation of transonic airfoil buffet at high Reynolds number, AIAA J. 56 (2018) 2372–2388.

[55] E. Degregori, J.W. Kim, Mitigation of transonic shock buffet on a supercritical airfoil through wavy leading edges, Phys. Fluids 33 (2021) 026104, https://doi.org/10.1063/5.0036821.

[56] P. Moise, M. Zauner, N. Sandham, Large-eddy simulations and modal reconstruction of laminar transonic buffet, J. Fluid Dyn. 944 (2022) A16, https://doi.org/10.1017/jfm.2022.471.

[57] P. Moise, M. Zauner, N. Sandham, S. Timme, W. He, Transonic buffet characteristics under conditions of free and forced transition, AIAA J. 61 (2023) 1061–1076, https://doi.org/10.1017/jfm.2022.471.

[58] A. D'Aguanno, F. Schrijer, B. van Oudheusden, Experimental investigation of the transonic buffet cycle on a supercritical airfoil, Exp. Fluids 621 (2021) 214, https://doi.org/10.1007/s00348-021-03319-z.

[59] A. D'Aguanno, F. Schrijer, B. van Oudheusden, Spanwise organization of upstream traveling waves in transonic buffet, Phys. Fluids 33 (2021) 106105, https://doi.org/10.1063/5.0062729.

[60] A. Accorinti, T. Baur, S. Scharnowski, C. Kahler, Experimental Investigation of Transonic Shock Buffet on an OAT15A Profile, AIAA Journal, 2022.

[61] K. Kokmanian, S. Scharnowski, C. Schafer, A. Accorinti, T. Baur, C. Kahler, Investigating the flow field dynamics of transonic shock buffet using particle image velocimetry, Exp. Fluids 63 (2022) 149, https://doi.org/10.1007/s00348-022-03499-2.

[62] D.C. Wilcox, Formulation of the $k-\omega$ turbulence model revisited, AIAA J. 46 (2008) 2823–2838, https://doi.org/10.2514/1.36541.

[63] R. Steijl, G. Barakos, K. Badcock, A framework for CFD anal-ysis of helicopter rotors in hover and forward flight, Int. J. Numer. Methods Fluids 51 (2006) 819–847, https://doi.org/10.1002/fld.1086.

[64] R. Steijl, G. Barakos, Sliding mesh algorithm for CFD analysis of helicopter rotor–fuselage aerodynamics, Int. J. Numer. Methods Fluids 58 (2008) 527–549, https://doi.org/10.1002/fld.1757.

[65] S. Osher, S. Chakravarthy, Upwind schemes and boundary conditions with applications to Euler equations in general geometries, J. Comput. Phys. 50 (1983) 447–481, https://doi.org/10.1016/0021-9991(83)90106-7.

[66] B. van Leer, Towards the ultimate conservative difference scheme. V. A second-order sequel to Godunov's method, J. Comput. Phys. 32 (1979) 101–136, https://doi.org/10.1016/0021-9991(79)90145-1.

[67] G. van Aldaba, B. van Leer, W. Roberts, A comparativestudy of computational methods in cosmic gas dynamics, Astron. Astrophys. 108 (1982) 76–84.

[68] O. Axelsson, Iterative Solution Methods, Cambridge University Press, 1994.

[69] L. Jacquin, P. Molton, S. Deck, B. Maury, D. Soulevant, An experimental study of shock oscillation over a transonic supercritical profile, in: AIAA Aerospace Sciences Meeting and Exhibit, Toronto, Ontario Canada, 2005.

[70] A. Petrocchi, G. Barakos, Buffet boundary estimation using a harmonic balance method, Aerosp. Sci. Technol. 132 (2023) 108086, https://doi.org/10.1016/j.ast.2022.108086.

[71] A. Petrocchi, G.N. Barakos, Transonic buffet simulation using a partially-averaged Navier-Stokes approach, in: ECCOMAS 2022, Oslo, Norway, 2022.

[72] P. Spalart, C. Rumsey, Effective inflow conditions for turbulence models in aerodynamic calculations, AIAA J. 45 (2007) 2544–2553, https://doi.org/10.1025/1.29737.

[73] F. Sartor, C. Mettot, D. Sipp, Stability, receptivity, and sensitivity analyses of buffeting transonic flow over a profile, AIAA J. 53 (2015) 1980–1993, https://doi.org/10.2514/1.J053588.

[74] Y. Tian, P. Feng, P. Liu, T. Hu, Q. Qu, Spoiler upward deflection on transonic buffet control of supercritical airfoil and wing, J. Aircr. 54 (2017) 1227–1231, https://doi.org/10.2514/1.C033574.

[75] N. Giannelis, O. Levinski, G. Vio, Influence of Mach number and angle of attack on the two-dimensional transonic buffet phenomenon, Aerosp. Sci. Technol. 78 (2018) 89–101, https://doi.org/10.1016/j.ast.2018.03.045.

[76] D.-M. Zimmermann, R. Mayer, T. Luiz, E. Kramer, Impact of model parameters of SALSA turbulence model on transonic buffet prediction, AIAA J. 56 (2018) 874–877, https://doi.org/10.2514/1.J056193.

[77] F. Plante, E. Laurendeau, Simulation of transonic buffet using a time-spectral method, AIAA J. 57 (2019) 1275–1277, https://doi.org/10.2514/1.J057224.

[78] Y. Zhao, Z. Dai, Y. Tian, Y. Xiong, Flow characteristics around airfoils near transonic buffet onset conditions, Chin. J. Aeronaut. 33 (2020) 1405–1420, https://doi.org/10.1016/j.cja.2019.12.022.

[79] S. Girimaji, Partially-averaged Navier-Stokes model for turbulence: a Reynolds-averaged Navier-Stokes to direct numerical simulation bridging method, J. Appl. Mech. 73 (2006) 413–421, https://doi.org/10.1115/1.2151207.

[80] S. Girimaji, Partially-averaged Navier-Stokes model for turbulence: fixed point analysis and comparison with unsteady partially averaged Navier Stokes, J. Appl. Mech. 73 (2006) 422–429, https://doi.org/10.1115/1.2173677.

[81] S. Lakshimpathy, S. Girimaji, Partially averaged Navier–Stokes (PANS) method for turbulence simulations: flow past a circular cylinder, J. Fluids Eng. 132 (2010) 121202, https://doi.org/10.1115/1.4003154.

[82] G. Gerolymos, I. Vallet, Influence of temporal integration and spatial discretization on hybrid rsm–vles computationss and iles, in: 18th AIAA Computational Fluid Dynamics Conference, Miami, FL, USA, 2007.

[83] B. Huang, G.-Y. Wang, Partially averaged Navier-Stokes method for time-dependent turbulent cavitating flows, J. Hydrodyn. 23 (2011) 26–33, https://doi.org/10.1016/S1001-6058(10)60084-4.

[84] R. Srinivasan, S. Girimaji, Partially-averaged Navier–Stokes simulations of high-speed mixing environmentediction, J. Fluids Eng. 136 (2011) 060903, https://doi.org/10.1115/1.4026234.

[85] B. Akula, P. Roy, P. Razi, S. Anderson, S. Girimaji, Partially-averaged Navier-Stokes (pans) simulations of lid-driven cavity flow—part 1: comparison with urans and les, in: S. G, et al. (Eds.), Progress in Hybrid RANS-LES Modelling, Springer International Publishing, 2015, pp. 359–369.

[86] F. Pereira, G. Vaz, L. Eca, An assessment of scale-resolving simulation models for the flow around a circular cylinder, Turbulence, Heat and Mass Transfer 8 (2015).

[87] M. Klapwijk, T. Lloyd, On the accuracy of partially averaged Navier–Stokes resolution estimates, Int. J. Heat Fluid Flow 80 (2019) 1–10, https://doi.org/10.1016/j.ijheatfluidflow.2019.108484.

[88] M. Klapwijk, T. Lloyd, G. Vaz, T. van Terwisga, Evaluation of scale-resolving simulations for a turbulent channel flow, Comput. Fluids 209 (2020) 104636, https://doi.org/10.1016/j.compfluid.2020.104636.

[89] S. Saroha, K. Chakraborty, S. Sinha, S. Lakshimpathy, Evaluation of PANS methodology with nonlinear eddy viscosity closure: flow past a heated sphere, J. Fluids Eng. 142 (2020) 091502, https://doi.org/10.1115/1.4047233.

[90] An OpenFOAM-Based Evaluation of PANS Methodology in Conjunction with Non-Linear Eddy Viscosity: Flow Past a Heated Cylinder

[91] T. Dzanic, S. Girimaji, F. Witherden, Partially-averaged Navier–Stokes simulations of turbulence within a high-order flux reconstruction framework, J. Comput. Phys. 456 (2022) 110992, https://doi.org/10.1016/j.jcp.2022.110992.

[92] H. Foroutan, S. Yavuzkurt, A partially-averaged Navier–Stokes model for the simulation of turbulent swirling flow with vortex breakdown, Int. J. Heat Fluid Flow 50 (2014) 402–416, https://doi.org/10.1016/j.ijheatfluidflow.2014.10.005.

[93] S. Krajnovic, G. Minelli, B. Basara, Partially-averaged Navier-Stokes simulations of flows around generic vehicle at yaw, in: SAE 2016 World Congress and Exhibition, Detroit, MI, USA, 2016.

[94] X. Han, S. Krajnovic, B. Basara, Study of active flow control for a simplified vehicle model using the PANS method, Int. J. Heat Fluid Flow 42 (2013) 139–150, https://doi.org/10.1016/j.ijheatfluidflow.2013.02.001.

[95] M. Mirzaei, S. Krajnovic, B. Basara, Partially-averaged Navier–Stokes simulations of flows around two different Ahmed bodies, Comput. Fluids 117 (2015) 273–286, https://doi.org/10.1016/j.compfluid.2015.05.010.

[96] G. Minelli, E. Hartono, V. Chernoray, L. Hjelm, B. Basara, S. Krajnovic, Validation of PANS and active flow control for a generic truck cabin, J. Wind Eng. Ind. Aerodyn. 171 (2017) 148–160, https://doi.org/10.1016/j.jweia.2017.10.001.

[97] A. Moosavifard, E. Kolb, M. Schafer, S. Jakirlic, Investigation of the PANS method for the prediction of aerodynamic noise around a circular cylinder, in: ECCOMAS 2022, Oslo, Norway, 2022.

[98] G. Nastac, A. Frendi, An investigation of scale-resolving turbulence models for supersonic retropropulsion flows, Fluids 7 (2022) 362, https://doi.org/10.3390/fluids7120362.

[99] A. Garbaruk, M. Strelets, J. Crouch, Effects of extended laminar flow on wing buffet-onset characteristics, AIAA J. 59 (2021) 2848, https://doi.org/10.2514/1.J060707.